



Astrochemical Diagnostics of the Isolated Massive Protostar G28.20-0.05

Downloaded from: <https://research.chalmers.se>, 2025-12-05 02:35 UTC

Citation for the original published paper (version of record):

Gorai, P., Law, C., Tan, J. et al (2024). Astrochemical Diagnostics of the Isolated Massive Protostar G28.20-0.05. *Astrophysical Journal*, 960(2). <http://dx.doi.org/10.3847/1538-4357/ad09bb>

N.B. When citing this work, cite the original published paper.



Astrochemical Diagnostics of the Isolated Massive Protostar G28.20-0.05

Prasanta Gorai^{1,2} , Chi-Yan Law^{1,3} , Jonathan C. Tan^{1,4} , Yichen Zhang^{5,4} , Rubén Fedriani^{6,1} , Kei E. I. Tanaka⁷ ,
Mélisse Bonfand⁴ , Giuliana Cosentino¹ , Diego Mardones⁸ , Maria T. Beltrán⁹ , and Guido Garay⁸

¹ Department of Space, Earth & Environment, Chalmers University of Technology, SE-412 96 Gothenburg, Sweden; prasanta.astro@gmail.com

² Department of Chemistry & Molecular Biology, Gothenburg University, Box 462, S-40530 Gothenburg, Sweden

³ European Southern Observatory, Karl-Schwarzschild-Strasse 2, D-85748 Garching, Germany

⁴ Department of Astronomy, University of Virginia, Charlottesville, VA 22904-4325, USA

⁵ Department of Astronomy, Shanghai Jiao Tong University, 800 Dongchuan Rd., Minhang, Shanghai 200240, People's Republic of China

⁶ Instituto de Astrofísica de Andalucía, CSIC, Glorieta de la Astronomía s/n, 18008 Granada, Spain

⁷ Department of Earth and Planetary Sciences, Tokyo Institute of Technology, Meguro, Tokyo, 152-8551, Japan

⁸ Departamento de Astronomía, Universidad de Chile, Las Condes, Santiago, Chile

⁹ INAF, Osservatorio Astrofisico di Arcetri, Largo E. Fermi 5, I-50125 Firenze, Italy

Received 2023 March 5; revised 2023 September 19; accepted 2023 November 2; published 2024 January 9

Abstract

We study the astrochemical diagnostics of the isolated massive protostar G28.20-0.05. We analyze data from Atacama Large Millimeter/submillimeter Array 1.3 mm observations with a resolution of $0''.2$ (~ 1000 au). We detect emission from a wealth of species, including oxygen-bearing (e.g., H_2CO , CH_3OH , CH_3OCH_3), sulfur-bearing (SO_2 , H_2S), and nitrogen-bearing (e.g., HNCO , NH_2CHO , $\text{C}_2\text{H}_3\text{CN}$, $\text{C}_2\text{H}_5\text{CN}$) molecules. We discuss their spatial distributions, physical conditions, correlation between different species, and possible chemical origins. In the central region near the protostar, we identify three hot molecular cores (HMCs). HMC1 is part of a millimeter continuum ring-like structure, is closest in projection to the protostar, has the highest temperature of ~ 300 K, and shows the most line-rich spectra. HMC2 is on the other side of the ring, has a temperature of ~ 250 K, and is of intermediate chemical complexity. HMC3 is further away, ~ 3000 au in projection, cooler (~ 70 K), and is the least line-rich. The three HMCs have similar mass surface densities (~ 10 g cm^{-2}), number densities ($n_{\text{H}} \sim 10^9$ cm^{-3}), and masses of a few solar masses. The total gas mass in the cores and in the region out to 3000 au is $\sim 25 M_{\odot}$, which is comparable to that of the central protostar. Based on spatial distributions of peak line intensities as a function of excitation energy, we infer that the HMCs are externally heated by the protostar. We estimate column densities and abundances of the detected species and discuss the implications for hot core astrochemistry.

Unified Astronomy Thesaurus concepts: Star formation (1569); Astrochemistry (75); Complex organic molecules (2256); Spectral line identification (2073); Massive stars (732); Interstellar medium (847)

1. Introduction

Massive stars play a significant role in the Universe: e.g., they create heavy elements; inject energy into the interstellar medium (ISM), and regulate surrounding star formation rates. They are thus crucial for controlling the evolution of galaxies. Despite their importance, it remains unclear how massive stars form. There are various theories in contention, such as core accretion (McKee & Tan 2003), competitive accretion (e.g., Bonnell et al. 2001; Grudić et al. 2022), and protostellar collisions (Bonnell et al. 1998; Bally et al. 2020). These different models involve different initial conditions and evolutionary paths of the massive protostellar core, which likely translate into different chemical evolution of the gas and dust since chemistry is highly sensitive to local physical conditions.

Many complex physical processes, such as infall, rotation, and outflows, are present, even from the earliest phases in high-mass young stellar objects (HMYSOs) and they can have a dramatic impact on astrochemical processes. A variety of species are commonly used as diagnostic tools to examine the nature of protostellar sources. For instance, CO is a good tracer of both lower-density ambient gas and protostellar outflows, C^{18}O is a good tracer of dense gas in the envelope, and SiO is a tracer of outflow shocks. Complex organic molecules (COMs;

≥ 6 atoms), primarily made of carbon atoms bonded with other elements and/or other carbon atoms, are common in the heated environments of HMCs that surround massive protostars, involving active grain surface and gas-phase chemistry. Understanding the chemistry of HMYSOs is important for inferring their physical conditions and chemical inventories.

More than 300 molecular species have been identified in the ISM and circumstellar shells [The Cologne Database for Molecular Spectroscopy (CDMS)].¹⁰ Among them, many species are COMs that have often been identified in HMCs (e.g., Herbst & van Dishoeck 2009; Jørgensen et al. 2020). HMCs are typically compact (≤ 0.1 pc), dense ($n_{\text{H}} \geq 10^6$ cm^{-3}), and hot ($\gtrsim 100$ K) structures that are associated with luminous infra-red (IR) sources and/or with ultracompact (UC) H II regions (e.g., Kurtz et al. 2000; van der Tak 2004; Cesaroni et al. 2010). Among the known COMs in HMCs, methanol is the most abundant and ubiquitous. Various other COMs, such as methyl formate (CH_3OCHO), dimethyl ether (CH_3OCH_3), acetone (CH_3COCH_3), acetaldehyde (CH_3CHO), glycolaldehyde (CH_2OHCHO), and ethylene glycol ($(\text{CH}_2\text{OH})_2$), have also been identified (e.g., Belloche et al. 2009; Rivilla et al. 2017; Pagani et al. 2019; Jørgensen et al. 2020). A variety of nitrogen-bearing complex species, such as formamide (NH_2CHO), vinyl cyanide ($\text{C}_2\text{H}_3\text{CN}$), ethyl cyanide ($\text{C}_2\text{H}_5\text{CN}$), methyl isocyanate (CH_3NCO), and isopropyl cyanide ($\text{iso-C}_3\text{H}_7\text{CN}$), have also been found (e.g., Belloche et al. 2017, 2019;

Original content from this work may be used under the terms of the [Creative Commons Attribution 4.0 licence](https://creativecommons.org/licenses/by/4.0/). Any further distribution of this work must maintain attribution to the author(s) and the title of the work, journal citation and DOI.

¹⁰ <https://cdms.astro.uni-koeln.de/classic/molecules>

Colzi et al. 2021). In addition to this chemical complexity, massive star-forming regions are often associated with crowded physical environments, which can make it difficult to interpret the line profiles, chemistry, spatial distributions, and chemical origins of all these molecular species. In particular, environmental effects are often invoked as the origin of chemical complexity and diversity. Thus, the study of isolated massive protostars, with minimal influence from other nearby stars, is of particular importance for the development and testing of astrochemical models.

G28.20-0.05 (hereafter G28.2) has been characterized as a shell-like hypercompact H II region, and an HMC is associated with it (Walsh et al. 2003; Sewilo et al. 2004; Qin et al. 2008). The distance has been estimated as 5.7 kpc (Sewilo et al. 2008), with this near-kinematic distance confirmed via proper-motion analysis (Law et al. 2022). The protostar has a luminosity of $1.4 \pm 0.5 \times 10^5 L_{\odot}$ (Law et al. 2022) (see also Hernández-Hernández et al. 2014; de la Fuente et al. 2020). Previous studies (e.g., Sollins et al. 2005) have suggested the presence of two components in the source: (i) an infalling equatorial gaseous torus, whose dense central region has become ionized; (ii) an extended molecular shell that is associated with a wide-angle outflow. Recent high-resolution Atacama Large Millimeter/submillimeter Array (ALMA) 1.3 mm observations indicate that G28.2 is relatively compact, isolated, and shows a ring-like structure. A detailed structural and kinematic study of this source from these data has been presented by Law et al. (2022). Based on the fragmentation properties measured in the 1.3 mm continuum image, they concluded that the protostar is forming in an isolated environment, i.e., with no compact, strong 1.3 mm continuum sources identified beyond the central core of $4''$ (0.11 pc) radius, and extending out over the ALMA field of view, i.e., a radius of $13''.5$ (0.37 pc). They identified a strong velocity gradient across the main continuum peak by investigating the H30 α first moment map and concluded that the emission is most likely to be tracing an ionized wind that is escaping from the massive protostar. They also detected a wide, extended protostellar outflow traced by CO(2–1), which also indicates that the star is still accreting. The best-fit spectral energy distribution models suggest a current protostellar mass of $43_{-27}^{+68} M_{\odot}$. From an initial inspection of the morphology of selected COMs, Law et al. (2022) concluded the source is chemically rich.

Previous studies detected various chemical species (e.g., CO, SO₂, OCS, NH₃, CH₃OH, CH₃CN) in G28.2 (e.g., Sewilo et al. 2008; Klaassen et al. 2011). However, their spatial distributions, column densities, and chemical origins were not investigated because of the relatively coarse angular resolution of the data ($1''.3$ to $1''.9$, i.e., 7500–10,700 au). Here, we present and analyze the 1.3 mm (ALMA Band 6) line data on scales down to $0''.2$ (0.0055 pc, i.e., 1140 au) of Law et al. (2022) to investigate the astrochemical inventory and implied diagnostics of G28.2.

This paper is organized as follows. In Section 2, we describe observational details and data analysis procedures. Results are presented in Section 3. We discuss several aspects of our results in Section 4 and conclude in Section 5.

2. Observations and Data Reduction

Observations of G28.2 were carried out with ALMA as a Cycle 3 project, covering two observational setups: compact (C) with angular resolution $\sim 0''.7$ and intermediate (I) with an angular resolution of $\sim 0''.2$ (PI: Y. Zhang; 2015.1.01454.S) and via Cycle 4 project with an extended (E) configuration with

an angular resolution of $\sim 0''.03$ (PI: J. Tan; 2016.1.00125.S). A detailed description of the observations, including observation time, number of antennas, baseline length, and maximum recoverable scale of different configurations, is given in Table 1 of Law et al. (2022). For the compact configuration, J1751+0939 (1.74 Jy) was used for bandpass and flux calibration, and J1830+0619 (0.31 Jy) was used as a phase calibrator. For the intermediate configuration, J1924-2914 (4.03 Jy) was used for bandpass and flux calibration, and J1851+0035 (0.24 Jy) was used as a phase calibrator. In each case, the source was observed with a single pointing and the primary beam size (half-power beamwidth) was $26''.9$. The observation was in band 6, covering a frequency range from 216–232 GHz. The same frequency ranges and spectral setups were used for the different configurations.

In the E configuration, we found that most of the molecular emissions are resolved out due to very high angular resolution (~ 200 au). The resolution of the I configuration is sufficient to spatially resolve all the observed molecular species. However, the maximum recoverable scale of the intermediate configuration is only $3''.4$, so molecular emissions on larger scales are filtered out. Therefore, we combined the C configuration with I. This C+I combined data is used for the analysis in this paper. The properties of these combined data are given in Table 1.

As part of the data reduction and analysis, raw data sets were processed through the standard ALMA calibration pipeline separately for C and I configurations by using CASA 4.5.3 and 4.7.0, respectively. All the analyses, such as continuum and spectral line analysis, were done using the CASA 5.6.1 software (McMullin et al. 2007). Since spectra toward G28.2 show various line emissions, it is essential to separate line and continuum information from the observed data set. To this aim, we selected line-free channels and applied first-order baseline fitting using the `uvcontsub` task in CASA. Following this method, we separated each spectral window into two data cubes: continuum and line emission for further analysis. To construct the continuum image, we sum line-free channels. We used the `concat` task for the combination of compact and intermediate configuration continuum and line data. We used `tclean` with Briggs weighting and a robust factor of 0.5 for both continuum and line imaging.

After separating the continuum and line data, we performed line identification on the cleaned spectral cubes using the Centre d’Analyse Scientifique de Spectres Infrarouges et Submillimétriques (CASSIS)¹¹ software, together with the Cologne Database for Molecular Spectroscopy (CDMS; Müller et al. 2001, 2005)¹² and Jet Propulsion Laboratory Pickett et al. (1998)¹³ databases. To identify molecular transitions in the observed spectra, we first identified peaks of emission that had intensities $\geq 3\sigma$, where σ is the rms noise (see Table 1). The identified peaks were then cross-matched against known transitions in the CDMS and JPL databases, with a focus on species already detected in the ISM. Note that the v_{LSR} of each hot core was determined from an average of identified strong lines from well-known species. Synthetic spectra from candidate species were also generated with a focus on conditions that are common to known hot cores (i.e., excitation temperatures up to several hundred kelvin), and any expected multiple transitions from a given species were searched for

¹¹ <http://cassis.irap.omp.eu>; Vastel et al. (2015).

¹² <https://www.astro.uni-koeln.de/cdms>

¹³ <http://spec.jpl.nasa.gov>

Table 1

Summary of the Observational Parameters of the Combined (Compact + Intermediate Configuration) ALMA Data, Including the Frequency Range, Spectral Resolution (Channel Spacing), Beam Size, and rms Noise of Each Spectral Window

Spw ^a	Frequency Range (MHz)	Channel Spacing (kHz)	Synthesized Beam ($\theta_{\text{major}} \times \theta_{\text{minor}}$)	rms ^b (mJy beam ⁻¹)
0	232,927.03–234,927.03	15625.00	0''20 × 0''18	0.7
1	231,586.78–232,055.53	488.28	0''19 × 0''18	3.2
2	230,296.19–230,764.94	488.28	0''18 × 0''17	5.4
3	218,713.74–218,655.14	122.07	0''21 × 0''20	7.2
4	218,393.79–218,335.20	122.07	0''21 × 0''20	6.2
5	219,513.82–219,455.22	122.07	0''20 × 0''19	5.6
6	220,277.12–220,218.53	122.07	0''21 × 0''20	6.7
7	220,218.53–216,912.63	488.28	0''21 × 0''20	3.8
8	216,685.46–216,451.08	488.28	0''22 × 0''21	4.2

Notes.^a Spw: spectral window;^b rms noise level measured in the channel maps of the continuum-subtracted data cubes.

(including allowing for potential line blending) in order to help make more secure detections.

3. Results

In Section 3.1, we first present an overview of the continuum image and the location of peak positions of certain species. These locations define three distinct HMCs in and around the massive protostar. In Section 3.2, we present the full spectra extracted from the three HMCs, which are used to explore the chemical inventory of the regions, including the velocity range of the detected species. Finally, in Section 3.3, we present integrated intensity maps of the main detected species, which more fully reveal their spatial structure. In Appendix A we also present the first moment maps of certain key species.

3.1. Continuum Image, Locations of Peak Molecular Line Emissions, and Identification of HMCs

Figure 1 shows the continuum image of G28.2 at 1.32 mm (225.62 GHz) with the combined configuration (C+I). This continuum emission, including its morphology at higher resolution, has been discussed by Law et al. (2022). A *ring-like* structure with a radius of about 2000 au was spatially resolved by Law et al. (2022) and is also discernible in the C+I data shown in Figure 1. From the millimeter continuum emission, after accounting for a contribution from free-free emission, Law et al. (2022) estimated the gas mass inside a radius of 0''5 to be about 30 M_{\odot} (for an assumed dust temperature of $T_d = 100$ K), corresponding to a mass surface density of $\Sigma_{\text{mm}} = 10.5 \text{ g cm}^{-2}$, i.e., $N_{\text{H}} = 4.5 \times 10^{24} \text{ cm}^{-2}$. This estimate is based on the assumption of optically thin dust emission, in which case a total (gas + dust) mass surface density can be derived from the 1.3 mm flux density via

$$\Sigma_{\text{mm}} = 369 \frac{F_{\nu} (\text{Jy})^2}{\Omega \kappa_{\nu,0.00638}} \frac{\lambda_{1.3}^3}{\kappa_{\nu,0.00638}} \times [\exp(0.111 T_{d,100}^{-1} \lambda_{1.3}^{-1}) - 1] \text{ g cm}^{-2}, \quad (1)$$

where F_{ν} is the total integrated flux over solid angle Ω and $\kappa_{\nu,0.00638} \equiv \kappa_{\nu}/0.00638 \text{ cm}^2 \text{ g}^{-1}$ is the dust absorption coefficient normalized to a fiducial value that has been derived assuming an opacity per unit dust mass of $0.899 \text{ cm}^2 \text{ g}^{-1}$ (i.e., from the moderately coagulated thin ice mantle model of

Ossenkopf & Henning 1994) and a gas-to-refractory-component-dust ratio of 141. In addition, in the above equation the dust temperature is normalized via $T_{d,100} \equiv T_d/100 \text{ K} = 1$ and the wavelength via $\lambda_{1.3 \text{ mm}} \equiv \lambda/1.3 \text{ mm} = 1$. Thus, the uncertainties in the estimate of Σ_{mm} are about a factor of 2, if the temperature is uncertain with the range from 50–200 K.

Here, we focus on the detection of various chemical species, their spatial distributions, column densities, abundances, excitation temperatures, and possible chemical origins of individual species. In the main continuum image, HMC1, HMC2, and HMC3 are marked with white crosses, representing locations where we find a concentration of molecular line emission, as described below.

Similar to Law et al. (2022), we perform a dendrogram analysis to study the different molecular structures toward G28.20-0.05 based on the integrated intensity (moment 0) maps of various species detected in spectra. We use the same dendrogram parameters as in (Law et al. 2022, and references therein), i.e., minvalue = 4σ (the minimum intensity considered in the analysis); mindelta = 1σ (the minimum spacing between isocontours); and minpix = 0.5 beam area (the minimum number of pixels contained within a structure). Here, $\sigma \equiv \text{rms}_{\text{chan}} \times \sqrt{N_{\text{chan}} dv}$, where rms_{chan} is the rms noise per channel (see Table 1), N_{chan} is the number of channels used to construct the moment 0 maps, and dv is the velocity resolution. For each dendrogram leaf, we identify the location of the peak intensity of its emission. We also measure the dendrogram leaf's average coordinate. From this analysis, we notice there are three main separate groupings of the peak positions. The average of these positions is used to define the locations of the HMCs, i.e., HMC1, HMC2, and HMC3.

We define circular apertures for these HMCs of 0''15 radius and will present the spectra of these regions in the next section. Here, we measure the continuum fluxes within these apertures and use this information to estimate the mass surface density (via Equation 1), and thus the total column density of H nuclei, $N_{\text{H}} = \Sigma/\mu_{\text{H}} = 4.27 \times 10^{23} (\Sigma/\text{g cm}^{-2}) \text{ cm}^{-2}$ (i.e., where the mass per H, accounting for $n_{\text{He}} = 0.1 n_{\text{H}}$, is $\mu_{\text{H}} = 1.4 m_{\text{H}} = 2.34 \times 10^{-24} \text{ g}$). We find values of $\Sigma_{1.3 \text{ mm}} \sim 10 \text{ g cm}^{-2}$ (all regions are within about a factor of 2 of this value, if using an estimate of T_d constrained from the observed HMCs lines) (see Table 2).

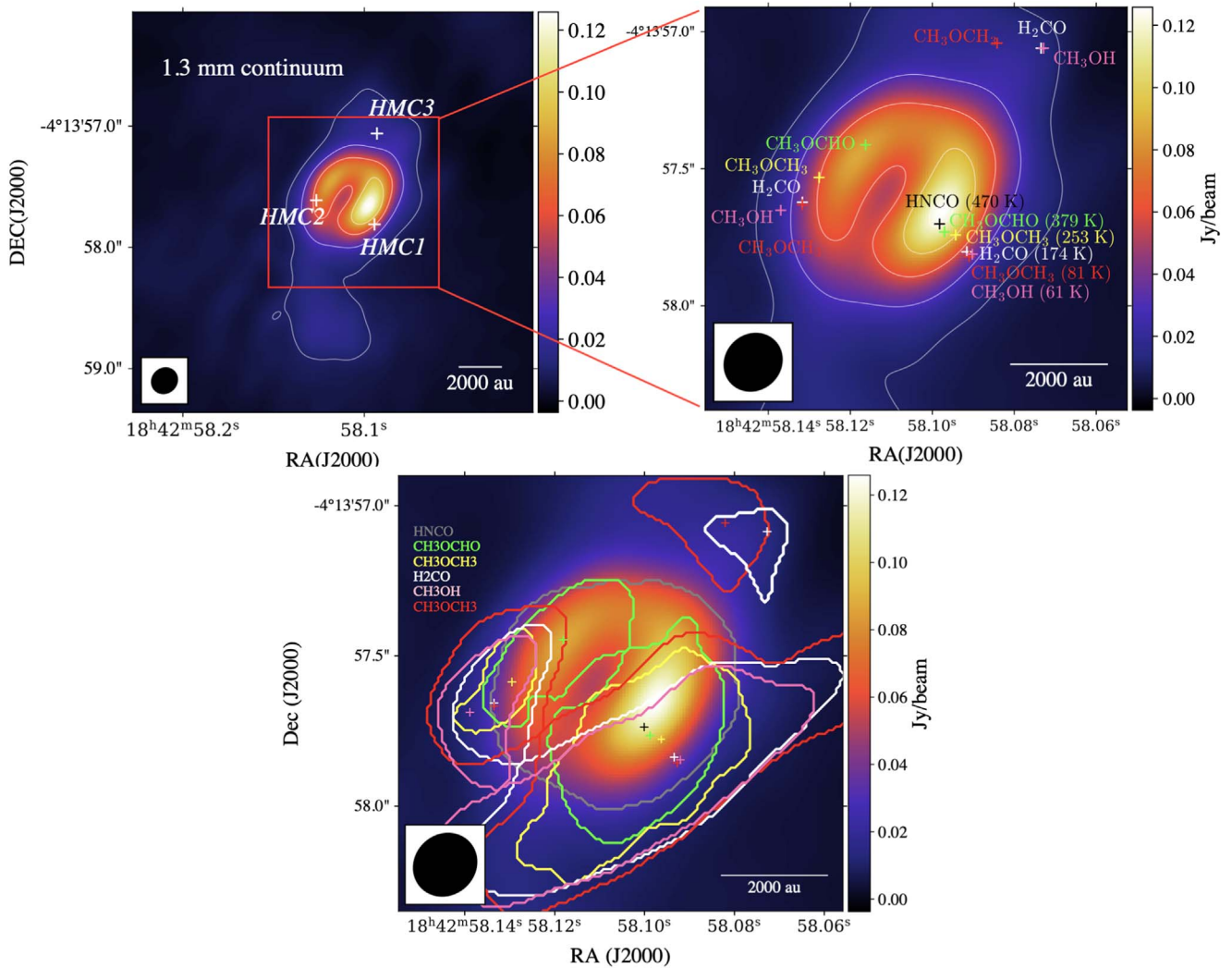


Figure 1. (a) Top left panel: continuum map of G28.2 obtained with ALMA at 230 GHz. Contour levels start at 3σ ($1\sigma = 1$ mJy beam $^{-1}$) and steps are in 3σ . The ellipse at the bottom-left corner of the image shows the synthesized beam ($0''.22 \times 0''.20$) with PA = -47° . Three white crosses represent the positions of HMC1, HMC2, and HMC3. (b) Top right panel: zoom-in of the central region, including locations of various molecular line emission peaks and associated upper-state energies. Note the implied temperature gradients along directions pointing away from the main millimeter continuum peak. (c) Bottom panel: same as (b), but now showing contours of different dendrogram leaves of several identified species (see the text).

Table 2
Positions, Mass Surface Densities, Column Densities, and Volume Densities of Millimeter Continuum Peaks and Identified HMCs

Source	$\alpha(\text{J2000})$	$\delta(\text{J2000})$	F_ν (mJy)	$\Sigma_{1.3\text{ mm}}$ (g cm $^{-2}$)	N_{H} (cm $^{-2}$)	n_{H} (cm $^{-3}$)
Cont. peak 1	18 $^{\text{h}}$ 42 $^{\text{m}}$ 58 $^{\text{s}}$.100	-4 $^{\circ}$ 13'57"641	138	42.16 (13.57)	1.80×10^{25} (5.80×10^{24})	4.23×10^9 (1.36×10^9)
Cont. peak 2	18 $^{\text{h}}$ 42 $^{\text{m}}$ 58 $^{\text{s}}$.120	-4 $^{\circ}$ 13'57"415	93	28.41 (9.15)	1.21×10^{25} (3.91×10^{24})	2.85×10^9 (9.19×10^8)
HMC1	18 $^{\text{h}}$ 42 $^{\text{m}}$ 58 $^{\text{s}}$.091	-4 $^{\circ}$ 13'57"841	47	14.39 (4.63)	6.15×10^{24} (1.98×10^{24})	1.44×10^9 (4.65×10^8)
HMC2	18 $^{\text{h}}$ 42 $^{\text{m}}$ 58 $^{\text{s}}$.134	-4 $^{\circ}$ 13'57"634	51	15.75 (6.05)	6.73×10^{24} (2.58×10^{24})	1.58×10^9 (6.08×10^8)
HMC3	18 $^{\text{h}}$ 42 $^{\text{m}}$ 58 $^{\text{s}}$.074	-4 $^{\circ}$ 13'57"058	17	10.51 (15.32)	4.49×10^{24} (6.55×10^{24})	1.05×10^9 (1.53×10^9)

Note. For continuum peaks 1 and 2 and HMC1 and HMC2, we remove 50% of the contribution of total measured flux, F_{ν} , due to an estimated contribution from free-free emission, and then use this value to estimate $\Sigma_{1.3\text{mm}}$, N_{H} , and n_{H} . The first value in these three columns assumes $T_d = 100$ K; the second value in parentheses assumes T_d is at a temperature estimated from the observed molecular lines, i.e., 300 K for HMC1, 250 K for HMC2, and 70 K for HMC3.

Under the assumption of spherical geometry of the core with a projected area equal to the defined circular aperture, we can also estimate the number density of H nuclei, n_{H} . Note, if the H is mostly in molecular form, then the actual particle number density (including He) is $n_{\text{tot,mol}} = 0.6n_{\text{H}}$. We find values of $n_{\text{H}} \sim 10^9 \text{ cm}^{-3}$ in the hot core regions. We note that, given the variation in millimeter continuum flux within the apertures, we

expect there are likely to be density (and temperature) variations within the defined core regions, so the above estimates should be recognized as average values in these regions.

In the zoom-in panels of Figure 1, we plot the peak positions for particular transitions of five species: HNC ($E_{\text{up}} = 470$ K); CH₃OCHO ($E_{\text{up}} = 379$ K); CH₃OCH₃ ($E_{\text{up}} = 254$ K); H₂CO ($E_{\text{up}} = 174$ K); and CH₃OH ($E_{\text{up}} = 61$ K). All five of the species

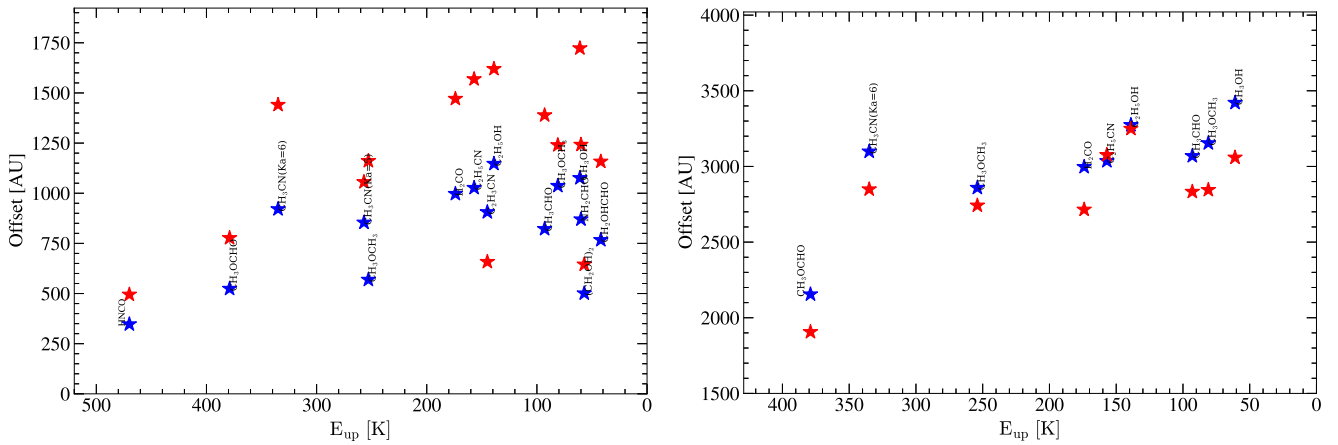


Figure 2. (a) Left panel: spatial offset between the molecular emission peak toward HMC1 and continuum peak 1. Blue stars are offsets of emission peaks within dendrogram leaves, while red stars are offsets of average positions of the leaves. (b) Right panel: as in (a), but now showing offsets between HMC2 line emission and continuum peak 1.

are detected in HMC1. Four of the species are detected in HMC2 (i.e., the highest energy species, HNC, is not detected). Three of the species are detected in HMC3 (i.e., the two highest energy species are not detected). Furthermore, within HMC1 we note a spatial sequence of the peak positions, moving along a vector away from the main millimeter continuum peak, which is thought to be the location of the massive protostar and main heating source (Law et al. 2022). A similar spatial sequence is seen in HMC2 and a hint of a sequence in HMC3. In Figure 2, we plot the offsets of peak emission from the main millimeter continuum source of a number of detected species in HMC1 and HMC2 as a function of E_{up} . We also plot the offsets to the locations of the average dendrogram positions. For both HMC1 and HMC2, there is a trend for the highest excitation transitions to be located closest to the main millimeter continuum peak. We consider this to be supporting evidence, in addition to the results of Law et al. (2022), that the main millimeter continuum peak is the location of the primary heating source in the region. Thus, HMC2 and HMC3 are not likely to be self-luminous, but rather are concentrations of molecular gas heated externally by the main continuum peak. This is also largely the case for the molecular gas of HMC1, which extends to the SW of the millimeter continuum peak, although it does have some material overlapping (in projection) with the peak of millimeter continuum emission that is the likely location of the protostar. We return to a general discussion of these results in Section 4.1.

3.2. Spectra

Spectra were extracted from a circular aperture of radius of $0''.15$ centered on the positions of HMC1, HMC2, and HMC3. Figure 3 shows these spectra. Table 3 summarizes all the detected species and their observed transitions. In total, 22 molecular species including isotopologues were detected, which include a wide variety of species, such as oxygen-bearing (H_2CO , CH_3OCH_3 , CH_3CHO , CH_2OHCHO , $\text{CH}_3\text{CH}_2\text{OH}$), nitrogen-bearing ($^{13}\text{CH}_3\text{CN}$, $\text{C}_2\text{H}_5\text{CN}$, $\text{C}_2\text{H}_3\text{CN}$, and NH_2CHO), and sulfur-bearing (SO_2 , H_2S) species (see Table 3). We note that HMC1 is the most chemically rich and its position is closest in projection to the expected location of the protostar, i.e., the main continuum peak. HMC2, which is on the NE side of the ring, has a similar set of emission lines as HMC1, but with evidence for somewhat cooler temperatures. Finally, HMC3 is cooler and less chemically rich than HMC1 and HMC2.

Most of the observed transitions exhibit a single Gaussian-like profile. Hence, we estimate the line width (FWHM or $\Delta\nu$) and the peak line intensity (I_{max}) of each transition by fitting a single Gaussian to each line profile. The parameters of all the observed transitions, such as quantum numbers ($J'_{K'aK'c} - J''_{K''aK''c}$), rest frequency (ν_0), upper state energy (E_u), line strength ($S \mu^2$), FWHM, and I_{max} are listed in Table 3.

The line centers of the transitions are found to be near a systematic velocity of 96.0 km s^{-1} for HMC1 and HMC3, while those of HMC2 are centered at 94.5 km s^{-1} . The average measured line widths of almost all species in HMC1 are $\sim 5 \text{ km s}^{-1}$, except for H_3O^+ , SiO , CO , H_2S , and one transition of $\text{C}_2\text{H}_3\text{CN}$, which are broader and possibly affected by the protostellar outflow. For HMC2 we find the average measured line widths of all the species are $\sim 3 \text{ km s}^{-1}$. H_3O^+ , SiO , CO , H_2S , and one transition of $\text{C}_2\text{H}_3\text{CN}$ are also broader in this region. For HMC3, the measured line widths of all species are similar to those found in HMC1.

3.3. Spatial Distribution of Molecules

We construct integrated intensity maps considering channels that cover the observed spectral profile of specific transitions, i.e., a velocity range of $\pm 4 \text{ km s}^{-1}$ from the line center. Figures 4–7 show the moment maps of all the species that are detected toward G28.2. These maps show a variety of emission peaks, including, as discussed above, varying spatial offsets from the continuum peaks.

3.3.1. C^{18}O Emission

$\text{C}^{18}\text{O}(2-1)$ ($E_{\text{up}} = 16 \text{ K}$) is detected in a region around the massive protostar extending about $6''$ in radius, i.e., about $34,000 \text{ au}$ or 0.17 pc . This is a region that we associate with the massive protostellar core, with the C^{18}O tracing the infall envelope. We note there is a decrement in the $\text{C}^{18}\text{O}(2-1)$ emission within the central ring-like continuum structure. While the C^{18}O emission exhibits substructure, this morphology is not especially correlated with the hot core positions.

3.3.2. H_2CO Emission

Two transitions of H_2CO ($J'_{K'aK'c} - J''_{K''aK''c} = 3_{21} - 2_{20}$; $9_{18} - 9_{19}$) are seen to be relatively strong toward G28.2 (see

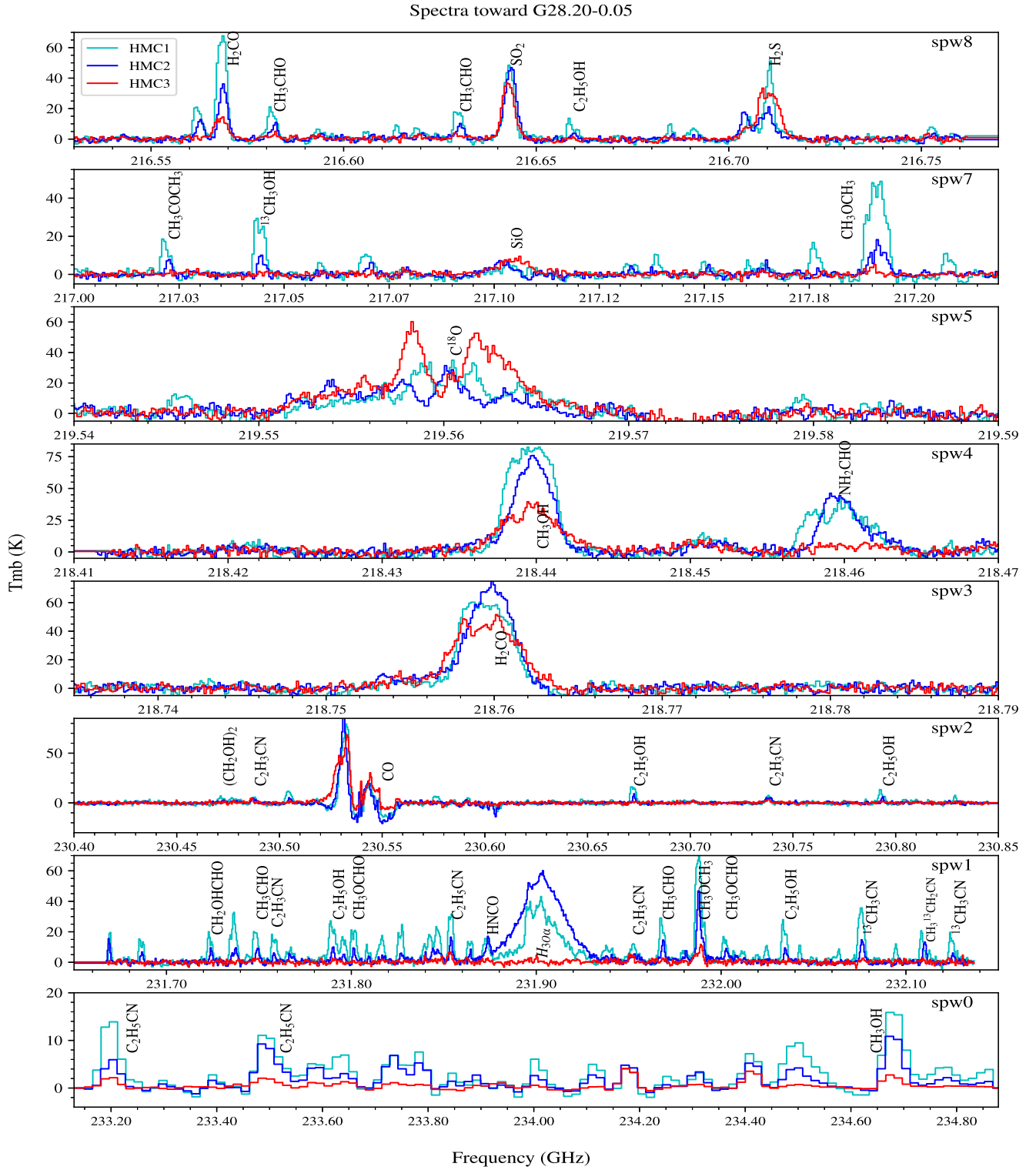


Figure 3. The continuum-subtracted spectra toward G28.20-0.05. All spectral windows except Spw6, where we did not find any clear evidence for molecular line emission, are shown, as labeled. Note that the displayed frequencies are in the rest frame of the source, i.e., after accounting for its $v_{\text{LSR}} = 95.6 \text{ km s}^{-1}$.

Table 3 and Figure 3). The FWHM of the higher excitation line ($E_{\text{up}} = 173 \text{ K}$) is about 0.5 km s^{-1} broader than that of the lower excitation line ($E_{\text{up}} = 68 \text{ K}$). The high-excitation transition shows different peak line intensities toward the three HMCs, i.e., highest toward HMC1 and lowest toward HMC3 (see Spw 8 panel of Figure 3). On the other hand, the low-excitation transition has its highest intensity toward HMC2 and lowest toward HMC3 (see the Spw 3 panel of Figure 3).

The moment 0 maps of these two transitions are shown in Figures 4(c) and 5(c). The low-excitation line of H_2CO has a more concentrated spatial distribution than that of C^{18}O . It shows enhancements near the continuum ring and a decrement within the ring. There is also a region of enhanced emission to the NE, which coincides with the direction of the near-facing outflow cavity as seen in high-velocity $^{12}\text{CO}(2-1)$ and $\text{SiO}(5-4)$ emission by Law et al. (2022). This could indicate a role

Table 3
Summary of the Line Parameters of Observed Transitions of Various Molecules toward G28.20-0.05

Species	$J'_{K'aK'c} - J''_{K''aK''c}$	Frequency (GHz)	E_u (K)	$S\mu^2$ (Debye ^b)	FWHM ^a (km s ⁻¹)	I_{\max}^1 (K)	FWHM ^b (km s ⁻¹)	I_{\max}^2 (K)	FWHM ^c (km s ⁻¹)	I_{\max}^3 (K)
CO	2-1	230.538000	16.59	0.02	D-C	D-C	D-C	D-C	D-C	D-C
C ¹⁸ O	2-1	219.560354	15.80	0.02	D-C	D-C	D-C	D-C	D-C	D-C
SiO	5-4	217.104980	31.25	47.99	5.23 ± 0.89	5.49 ± 0.81	8.01 ± 0.71	6.02 ± 0.46	11.25 ± 0.69	7.89 ± 0.37
SO ₂	22 _{2,20} -22 _{2,21}	216.643303	248.44	35.25	4.81 ± 0.10	46.99 ± 0.81	4.23 ± 0.09	46.98 ± 0.82	5.01 ± 0.11	37.99 ± 0.75
H ₂ S	2 _{2,0} -2 _{1,1}	216.710436	83.98	2.06	3.47 ± 0.16	47.36 ± 1.83	6.94 ± 0.49	17.65 ± 1.01	9.19 ± 0.48	31.43 ± 1.30
H ₂ CO	3 _{2,1} -2 ₀	218.760066	68.11	9.06	4.50 ± 0.13	64.33 ± 1.58	4.24 ± 0.07	71.83 ± 0.97	6.11 ± 0.15	47.53 ± 0.97
	9 _{1,8} -9 _{1,9}	216.568651	173.99	3.74	3.74 ± 0.19	72.39 ± 3.18	3.50 ± 0.08	35.75 ± 0.67	5.31 ± 0.24	14.03 ± 0.54
CH ₃ OH	4 _{2,3} -5 _{1,4} A, vt = 0	234.683370	60.92 ^d	4.48	D-L	D-L	D-L	D-L	D-L	D-L
	5 _{4,2} -6 _{3,3} A, vt = 0	234.698500	122.72 ^d	1.84	D-L	D-L	D-L	D-L	D-L	D-L
	4 _{-2,3} -3 _{-1,2} E, vt = 0	218.440060	45.46 ^e	13.91	4.46 ± 0.15	88.69 ± 2.42	3.85 ± 0.08	73.93 ± 1.29	5.90 ± 0.15	33.75 ± 0.71
¹³ CH ₃ OH	14 _{1,13} -13 _{2,12}	217.044616	254.25	5.79	3.90 ± 0.50	28.79 ± 3.11	2.38 ± 0.43	9.90 ± 1.53	ND	ND
C ₂ H ₃ CN	25 _{0,25} -24 _{0,24}	230.738557	145.54	1089.83	2.91 ± 0.27	7.68 ± 0.62	5.04 ± 0.44	5.03 ± 0.37	3.87 ± 0.51	3.02 ± 0.33
	24 _{1,23} -23 _{1,22}	230.487936	141.25	1044.95	2.82 ± 0.53	6.23 ± 0.97	3.71 ± 0.67	4.11 ± 0.60	1.87 ± 0.31	5.06 ± 0.71
	24 _{2,22} -23 _{2,21}	231.952331	146.84	1040.74	6.97 ± 0.43	10.46 ± 0.55	8.11 ± 1.04	4.31 ± 0.44	3.67 ± 0.62	5.05 ± 0.73
	26 _{0,26} -25 _{1,25}	231.756777	157.04	48.35	4.57 ± 0.60	16.17 ± 1.73	1.86 ± 0.26	6.29 ± 0.76	ND	ND
	23 _{5,19} -22 _{5,18}	218.451297	179.80	956.77	3.30 ± 0.20	11.63 ± 0.60	4.57 ± 0.65	6.66 ± 0.57	4.00 ± 0.46	7.20 ± 0.68
	23 _{8,15} -28 _{1,14}	218.421801	263.81	882.78	4.98 ± 2.93	5.08 ± 0.85	ND	ND	ND	ND
CH ₃ CHO	12 _{3,9} -11 _{3,8}	231.968385	92.62	142.33	4.14 ± 0.36	27.14 ± 1.99	2.57 ± 0.18	14.41 ± 0.82	ND	ND
	12 _{3,10} -11 _{3,9}	231.748719	92.51	141.14	3.94 ± 0.30	21.37 ± 1.37	2.98 ± 0.23	9.12 ± 0.61	ND	ND
	11 _{1,10} -10 _{1,9}	216.581930	64.87	137.93	3.62 ± 0.29	19.41 ± 1.29	2.99 ± 0.39	9.45 ± 1.05	ND	ND
	11 _{1,10} -10 _{1,9}	216.630234	64.81	137.84	3.38 ± 0.42	19.59 ± 2.1	3.31 ± 0.39	9.35 ± 0.94	ND	ND
C ₂ H ₅ CN	27 _{1,27} -26 _{1,26}	231.854212	157.73	399.21	3.74 ± 0.31	34.10 ± 2.40	2.34 ± 0.18	15.69 ± 1.01	3.18 ± 0.25	6.99 ± 0.47
	27 _{0,27} -26 _{0,26}	231.990409	157.71	399.25	2.66 ± 0.42	22.21 ± 2.20	3.13 ± 0.22	16.28 ± 0.39	3.02 ± 0.17	11.60 ± 0.76
	26 _{6,20} -25 _{6,19}	233.207380	191.00	364.54	D-L	D-L	D-L	D-L	D-L	D-L
	26 _{5,21} -25 _{5,20}	233.498300	178.86	370.75	D-L	D-L	D-L	D-L	D-L	D-L
CH ₃ ¹³ CH ₂ CN*	26 _{6,20} -25 _{6,19}	232.109851	189.24	358.46	D-B(a)	D-B(a)	ND	ND	ND	ND
	26 _{15,11} -26 _{15,10}	231.980825	393.00	252.61	4.55 ± 0.90	7.26 ± 0.77	ND	ND	ND	ND
CH ₃ OCH ₃	22 _{4,19} -22 _{3,20} AE	217.189669	253	122.88	4.46 ± 0.62	37.88 ± 6.41	2.04 ± 0.23	10.59 ± 0.91	1.98 ± 0.97	4.77 ± 1.30
	22 _{4,19} -22 _{3,20} EE	217.191400	253	327.70	3.06 ± 1.36	23.71 ± 5.73	1.58 ± 0.13	16.83 ± 1.21	1.63 ± 1.07	3.10 ± 1.88
	22 _{4,19} -22 _{3,20} AA	217.193132	253	204.82	3.40 ± 0.69	29.84 ± 7.85	2.93 ± 0.29	11.20 ± 0.78	ND	ND
	13 _{0,13} -12 _{1,12} AE	231.987783	81	169.90	4.94 ± 0.34	72.32 ± 4.11	3.53 ± 0.33	43.73 ± 3.47	3.87 ± 0.55	5.46 ± 0.41
	13 _{0,13} -12 _{1,12} EE	231.987858	81	271.84	D-M	D-M	D-M	D-M	D-M	D-M
	13 _{0,12} -12 _{0,12} AA	231.987932	81	101.93	D-M	D-M	D-M	D-M	D-M	D-M
HNCO	28 _{1,28} -29 _{0,29}	231.873255	470.00	26.24	5.43 ± 0.28	15.17 ± 0.66	4.28 ± 0.35	15.10 ± 0.88	ND	ND
NH ₂ CHO	10 _{1,9} -9 _{1,8}	218.459213	60.81	129.35	6.06 ± 0.31	35.62 ± 1.41	4.01 ± 0.15	44.20 ± 0.98	ND	ND
g-C ₂ H ₅ OH	13 _{2,11} -12 _{2,10}	230.672554	138.62	20.28	3.72 ± 0.34	17.06 ± 1.35	1.56 ± 0.11	8.98 ± 0.54	ND	ND
	8 _{4,5} -7 _{3,5}	216.659683	106.30	5.00	D-B(b)	D-B(b)	ND	ND	ND	ND
	6 _{5,1} -5 _{4,1}	230.793763	104.80	5.55	3.80 ± 0.47	11.48 ± 1.22	1.53 ± 0.20	6.22 ± 0.70	ND	ND
t-C ₂ H ₅ OH	18 _{5,14} -18 _{4,15}	232.034630	175.29	18.61	4.04 ± 0.45	24.90 ± 0.35	2.34 ± 0.23	9.14 ± 0.75	ND	ND
	22 _{5,18} -22 _{4,19}	231.790000	244.54	23.10	5.67 ± 0.53	24.58 ± 1.75	2.36 ± 0.08	10.14 ± 0.27	ND	ND
¹³ CH ₃ CN	13 ₅ -12 ₅	232.125129	256.88	340.77	3.85 ± 0.37	17.55 ± 1.41	2.02 ± 0.32	5.90 ± 0.80	ND	ND
	13 ₆ -12 ₆	232.077200	335.51	629.49	D-B(c)	D-B(c)	ND	ND	ND	ND
	13 ₇ -12 ₇	232.002069	428.41	283.97	D-B(d)	D-B(d)	ND	ND	ND	ND
	13 ₈ -12 ₈	231.955371	535.54	248.44	D-B(e)	D-B(e)	ND	ND	ND	ND
	13 ₉ -12 ₉	231.881500	656.88	416.44	D-B(f)	D-B(f)	ND	ND	ND	ND
CH ₂ OHCHO	8 _{6,2} -7 _{5,3}	231.724332	41.85	29.85	1.87 ± 0.12	13.22 ± 0.44	1.94 ± 0.20	8.99 ± 18.61	ND	ND
	8 _{6,3} -7 _{5,2}	231.723226	41.85	29.85	1.83 ± 0.11	19.76 ± 0.43	D-M	D-M	ND	ND

Table 3
(Continued)

Species	$J'_{K'aK'c} - J''_{K''aK''c}$	Frequency (GHz)	E_u (K)	$S\mu^2$ (Debye ^b)	FWHM ^a (km s ⁻¹)	I_{\max}^1 (K)	FWHM ^b (km s ⁻¹)	I_{\max}^2 (K)	FWHM ^c (km s ⁻¹)	I_{\max}^3 (K)
g' Gg (CH ₂ OH) ₂	14 _{3,11} –13 _{2,12}	230.576100	57.10	15.35	3.38 ± 0.70	7.24 ± 1.25	ND	ND	ND	ND
g' Ga (CH ₂ OH) ₂	21 _{4,17} –20 _{4,16}	230.472500	124.25	598.99	1.80 ± 0.11	3.5 ± 0.21	ND	ND	ND	ND
CH ₃ OCHO	19 _{11,8} –18 _{11,7}	232.002595	379.73	33.67	4.48 ± 0.45	15.70 ± 1.11	2.94 ± 0.23	8.57 ± 0.50	ND	ND
	19 _{16,3} –18 _{16,3}	231.800934	469.99	14.78	2.71 ± 0.26	21.87 ± 0.78	D-M	D-M	ND	ND
	19 _{17,2} –18 _{17,1}	231.801954	492.08	10.14	1.59 ± 0.13	19.37 ± 1.24	1.72 ± 0.29	9.99 ± 1.46	ND	ND
	35 _{9,27} –35 _{8,28}	217.165400	418.42	9.70	D-B(g)	D-B(g)	D-B(g)	D-B(g)	ND	ND
H ₂ ¹³ CCO*	11 _{1,10} –10 _{1,9}	217.149700	75.60	66.18	2.06 ± 0.11	7.14 ± 0.181	1.29 ± 0.09	5.36 ± 0.31	ND	ND
CH ₃ COCH ₃	19 _{4,16} –18 _{3,15} , EE	217.022508	115.49	2042.48	3.04 ± 0.40	176.43 ± 0.43	1.94 ± 0.18	8.39 ± 0.67	ND	ND
	19 _{3,16} –18 _{4,15} , AA	217.070500	115.43	1276.35	4.42 ± 0.34	10.77 ± 0.69	2.16 ± 0.55	5.98 ± 1.25	ND	ND

Note. *Tentative detection; ND: nondetection of transition; D-C: detection of transition, but line parameters have not been measured due to complex line profiles; D-L: detection of transition, but in Spw 0 with low (~ 20 km s⁻¹) velocity resolution, so no measurement of line parameters; D-M: detection of a multiplet, but without resolution of the individual lines; D-B(a): detection, but blended with CH₃CHO; D-B(b) detection, but blended with c-C₃H; D-B(c): detection, but blended with C₂H₅OH; D-B(d): detection, but blended with C₃HD; D-B(e): detection, but blended with C₂H₃CN; D-B(f): detection, but blended with H30 α ; D-B(g): detection, but blended with CH₃COCH₃. RMS noise for different spectral windows varies between 0.94 and 2.3 K. Integrated intensity can be estimated via $\int T_{\text{mb}} d\nu = 1.064 \times I_{\max} \times \text{FWHM}$.

^a Line parameters measured toward HMC1.

^b Line parameters measured toward HMC2.

^c Line parameters measured toward HMC3.

^d High-excitation methanol ($E_{\text{up}} = 60.92$ K and 122.72 K).

^e Low-excitation methanol ($E_{\text{up}} = 45.46$ K).

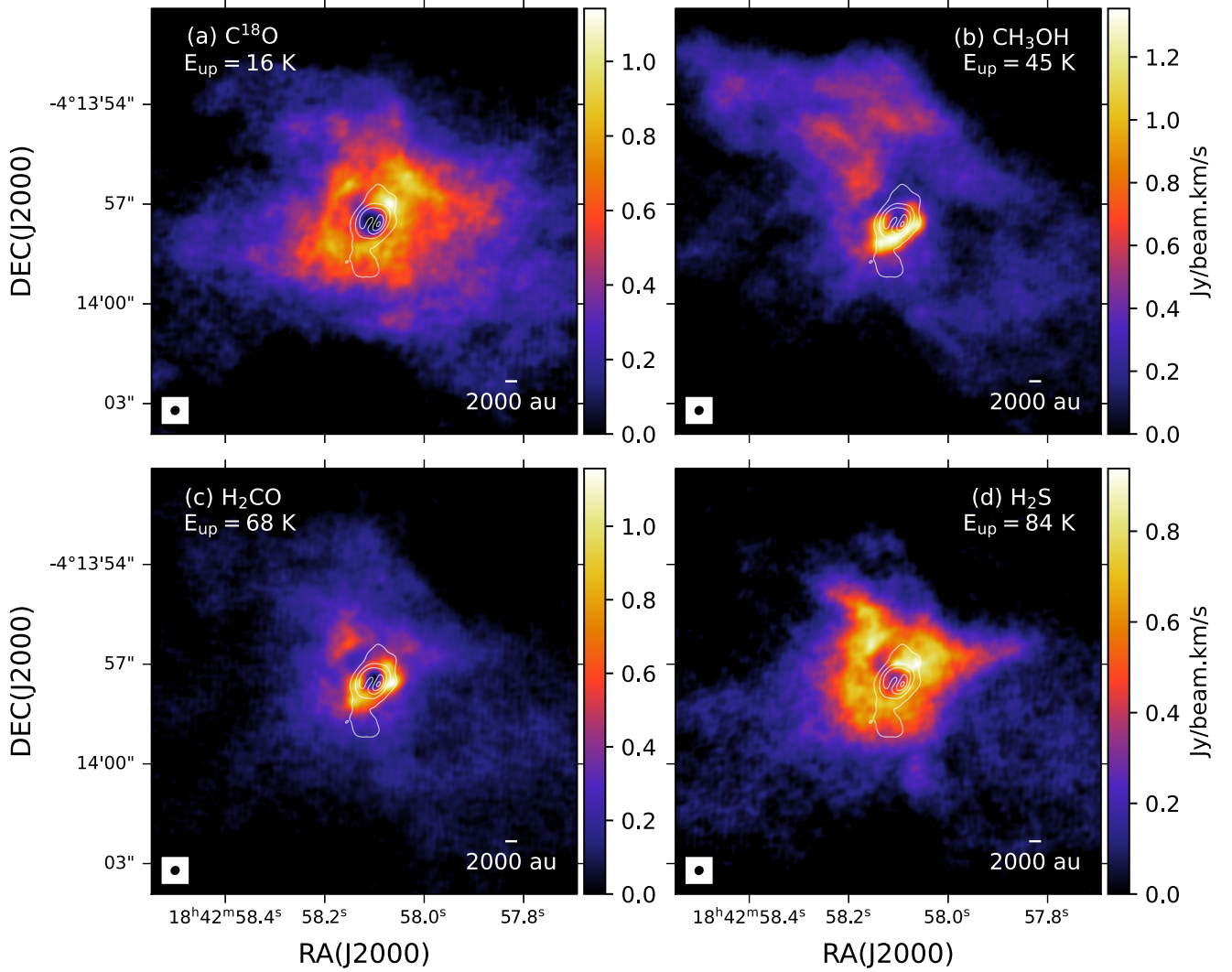


Figure 4. Moment 0 maps of species showing a widespread distribution: (a) C^{18}O ($2-1$; $E_{\text{up}} = 16$ K), (b) CH_3OH ($E_{\text{up}} = 45$ K), (c) H_2CO ($E_{\text{up}} = 68$ K), and (d) H_2S ($E_{\text{up}} = 84$ K). The white contours show 1.32 mm continuum emission (same contours as in Figure 1).

for outflow-driven shocks in liberating H_2CO into the gas phase (see Section 4.4 for further discussion). The emission peaks of the high-excitation line of H_2CO are more spatially concentrated and are seen mainly toward HMC1 and HMC2, but also, faintly, toward HMC3.

H_2CO is expected to be mainly produced on grain surfaces via two successive hydrogen addition reactions with $\text{CO} \xrightarrow{\text{H}} \text{HCO} \xrightarrow{\text{H}} \text{H}_2\text{CO}$. It sublimates to the gas phase when conditions become warmer. Figure A1(a) depicts the moment 1 map of the high-excitation transition of H_2CO . The velocity field shows a complex structure, with no clear evidence for a simple gradient that might indicate rotation orthogonal to the known outflow direction (NE–SW axis).

3.3.3. CH_3OH Emission

Two transitions of CH_3OH (with $E_{\text{up}} = 45$ and 61 K) and one transition of $^{13}\text{CH}_3\text{OH}$ (with $E_{\text{up}} = 254$ K) are detected toward G28.2 (see Table 3). Figure 4(b), and Figures 5(a) and (f) show moment 0 maps of these transitions. The spatial distribution of the 61 K transition of methanol is similar to that of the high-excitation line ($E_{\text{up}} = 173$ K) of H_2CO . Methanol is expected to be mainly produced on the surface of grains via

four successive hydrogen additions with CO ($\text{CO} \xrightarrow{\text{H}} \text{HCO} \xrightarrow{\text{H}} \text{H}_2\text{CO} \xrightarrow{\text{H}} \text{CH}_3\text{O} \xrightarrow{\text{H}} \text{CH}_3\text{OH}$). The morphology of methanol and formaldehyde emissions are similar, which is consistent with their similar chemical origin. Most likely they are directly evaporated from the grain mantles via various thermal and nonthermal desorption processes.

The emission of the low-excitation CH_3OH transition ($E_{\text{up}} = 46$ K) shows a spatial distribution that is similar to that of the low-excitation line of H_2CO . This indicates that these species are being liberated into the gas phase on scales of at least $\sim 10^4$ au. Extension in the outflow direction to the NE may also indicate a role for shocks in promoting this desorption (see Section 4.4 for further discussion).

3.3.4. H_2S Emission

One transition ($E_{\text{up}} = 84$ K) of hydrogen sulfide (H_2S) is detected toward G28.2 (see Table 3). Figure 4(d) depicts the moment 0 map of H_2S . We find the H_2S emission is extended, i.e., with some similarities to the C^{18}O and low-excitation lines of H_2CO and CH_3OH , including potential enhancement in the NE outflow direction. The different spatial distribution of H_2S

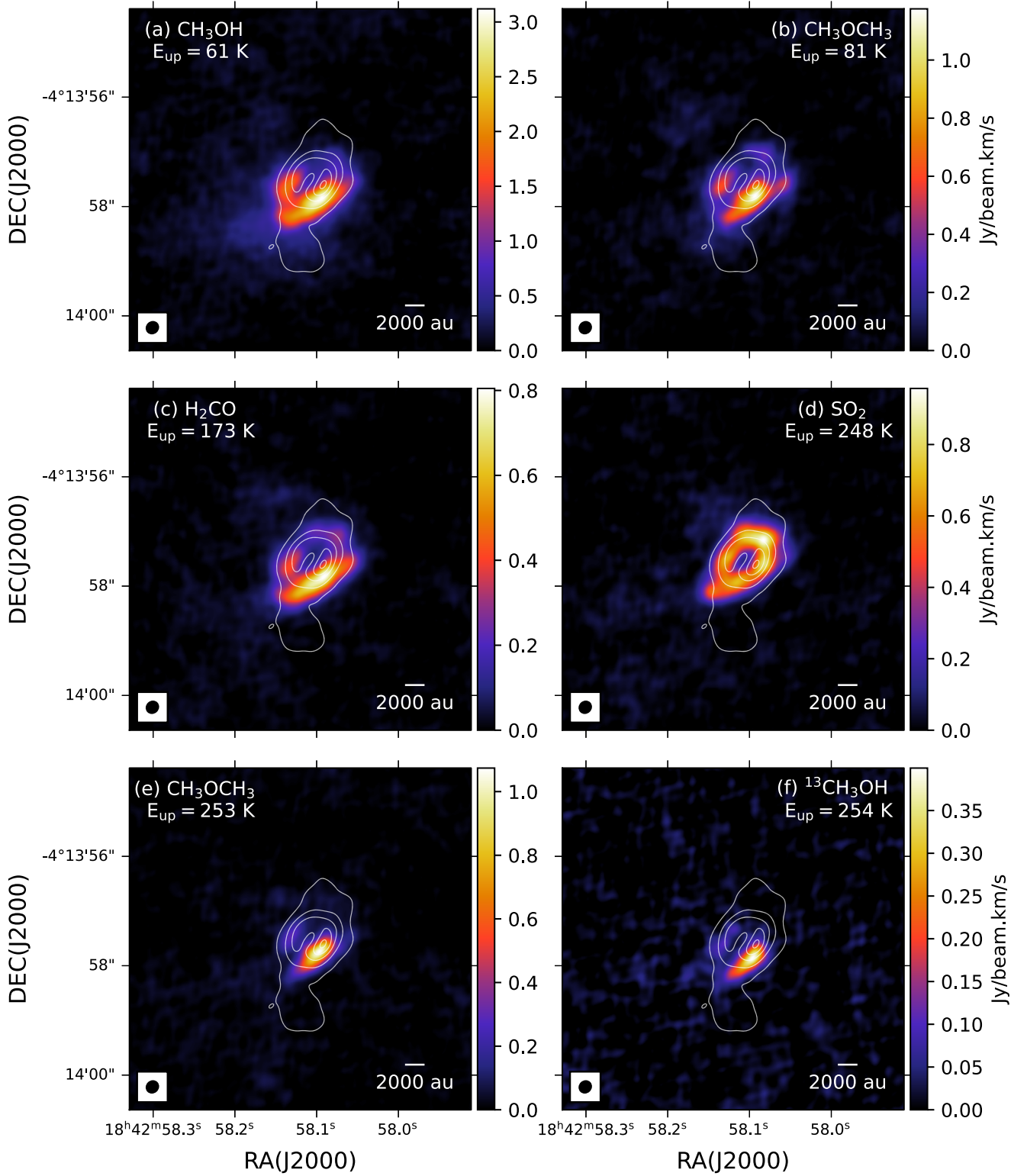


Figure 5. Moment 0 maps of O-bearing species showing a concentrated distribution: (a) CH_3OH ($E_{\text{up}} = 68 \text{ K}$), (b) CH_3OCH_3 ($E_{\text{up}} = 81 \text{ K}$), (c) H_2CO ($E_{\text{up}} = 173 \text{ K}$), (d) SO_2 ($E_{\text{up}} = 248 \text{ K}$), (e) CH_3OCH_3 ($E_{\text{up}} = 253 \text{ K}$), and (f) $^{13}\text{CH}_3\text{OH}$ ($E_{\text{up}} = 254 \text{ K}$). The white contours show 1.32 mm continuum emission (same contours as in Figure 1).

compared to SO_2 (discussed below) indicates different chemical origins of these S-bearing species.

3.3.5. SO_2 Emission

One transition of sulfur dioxide (SO_2) is detected ($J'_{K'aK'c} - J''_{K''aK''c} = 22,2,20 - 22,2,21$; $E_{\text{up}} = 253 \text{ K}$) toward G28.2. Figure 3

shows the observed line profile of SO_2 . The zeroth-order moment map of SO_2 is depicted in Figure 5(d). The emission peak of this species coincides with the ring-like continuum structure of the source as seen for $\text{H}30\alpha$ (Law et al. 2022). The first-order moment map is shown in Figure A1. It reveals quite complex kinematics in the region around the continuum ring, with velocity differences of several kilometers per second.

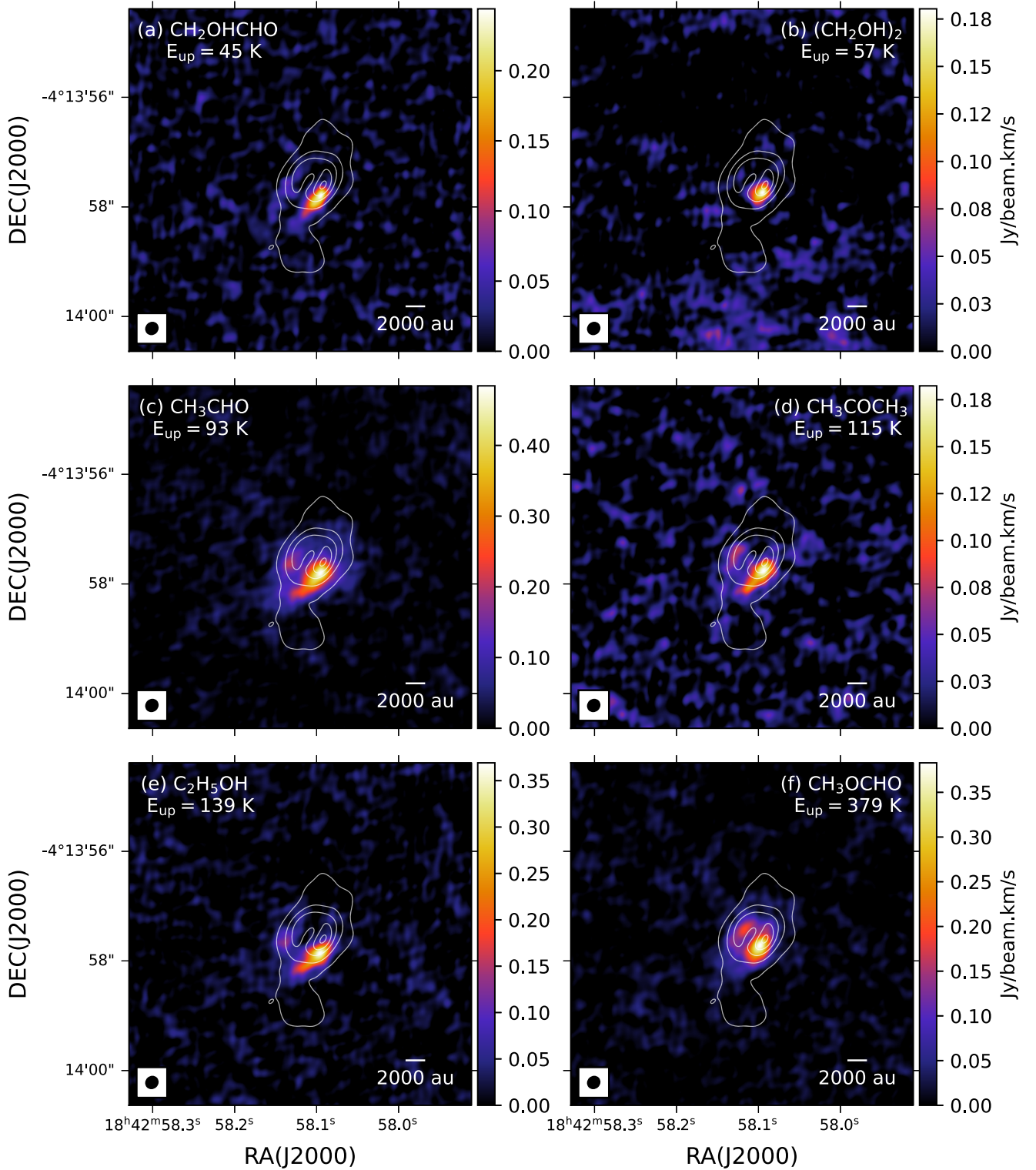


Figure 6. Moment 0 maps of additional O-bearing species showing a concentrated distribution: (a) CH_2OHCHO ($E_{\text{up}} = 45$ K), (b) $(\text{CH}_2\text{OH})_2$ ($E_{\text{up}} = 57$ K), (c) CH_3CHO ($E_{\text{up}} = 93$ K), (d) CH_3COCH_3 ($E_{\text{up}} = 115$ K), (e) $\text{C}_2\text{H}_5\text{OH}$ ($E_{\text{up}} = 139$ K), and (f) CH_3OCHO ($E_{\text{up}} = 379$ K). The white contours show 1.32 mm continuum emission (same contours as in Figure 1).

SO_2 is often observed to be associated with UC H II regions and is thought to be formed in the high-temperature gas phase through atomic sulfur or sulfur-bearing species evaporated from the grain mantles (Minh 2016b). The similar spatial distribution of SO_2 and $\text{H}30\alpha$ in G28.2 may indicate that SO_2 is formed in the high-temperature gas.

3.3.6. CH_3OCH_3 Emission

Two transitions of dimethyl ether (CH_3OCH_3) are detected toward G28.2. One is of relatively low excitation ($E_{\text{up}} = 81$ K) and the other is of higher excitation ($E_{\text{up}} = 253$ K) (see Table 3). The spectra of these two transitions are

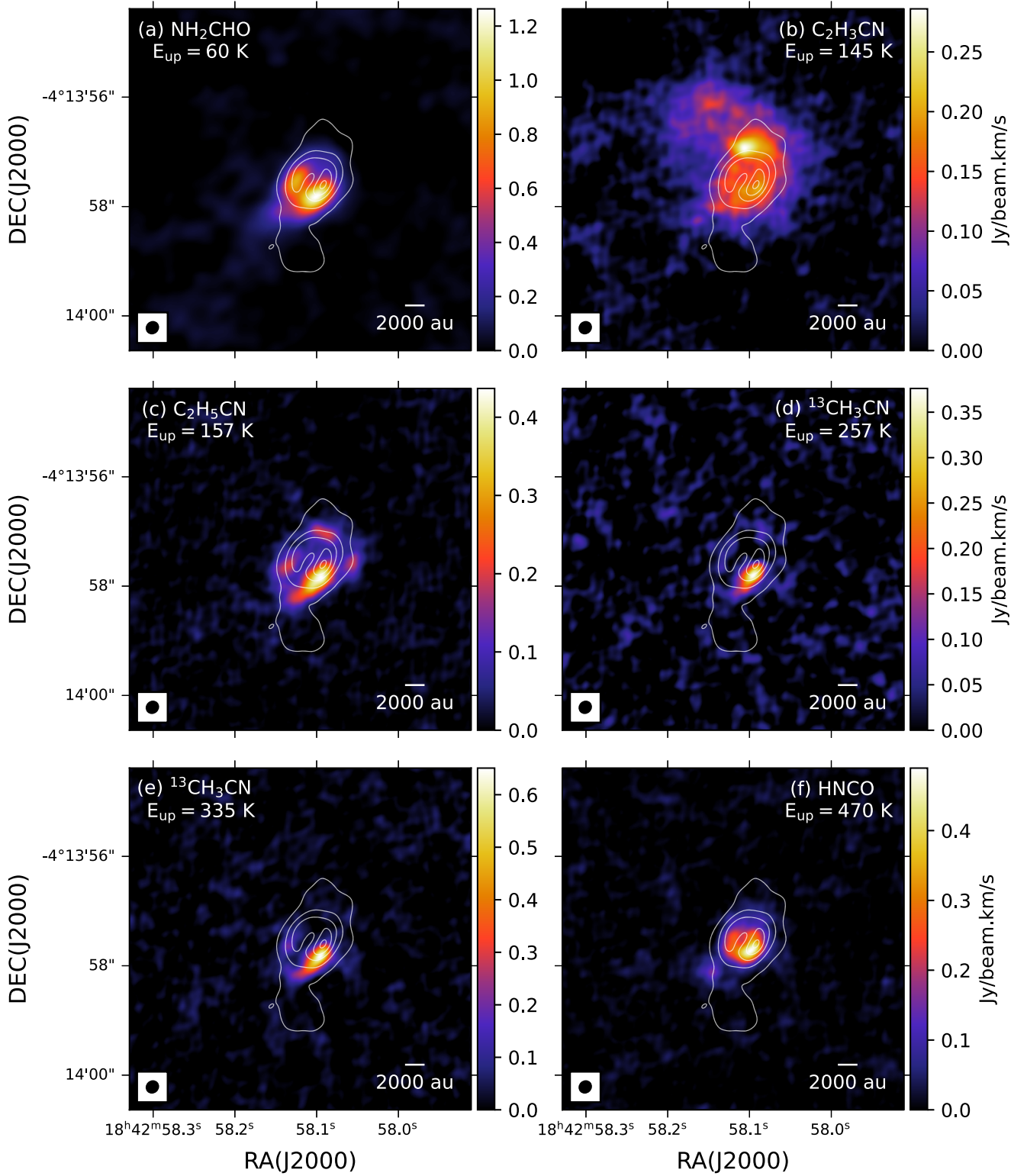


Figure 7. Moment 0 maps of N-bearing species showing a concentrated distribution: (a) NH_2CHO ($E_{\text{up}} = 60$ K), (b) $\text{C}_2\text{H}_3\text{CN}$ ($E_{\text{up}} = 145$ K), (c) $\text{C}_2\text{H}_5\text{CN}$ ($E_{\text{up}} = 157$ K), (d) $^{13}\text{CH}_3\text{CN}$ ($13_5 - 12_5$; $E_{\text{up}} = 257$ K), (e) $^{13}\text{CH}_3\text{CN}$ ($13_6 - 12_6$; $E_{\text{up}} = 335$ K), and (f) HNCO ($E_{\text{up}} = 470$ K). The white contours show 1.32 mm continuum emission (same contours as in Figure 1).

shown in Figure 3. The moment 0 maps are shown in Figures 5(b) and (e). These show the brightest emission toward HMC1, fainter emission toward HMC2, and only very faint emission in the low-excitation transition toward HMC3. In general, the morphology of CH_3OCH_3 is similar to those of the high E_{up} transitions of CH_3OH , CH_3CHO ,

and $\text{C}_2\text{H}_5\text{OH}$, which again indicates their similar chemical origins.

CH_3OCH_3 is expected to be mainly produced on the surfaces of grain mantles via radical–radical reaction between CH_3 and CH_3O (e.g., Garrod & Herbst 2006; Garrod 2013). It could also be produced in the gas phase via ion–molecule reactions in two

steps starting from the reaction between protonated methanol, CH_3OH_2^+ , and CH_3OH and finally the reaction between $(\text{CH}_3)_2\text{OH}^+$ and NH_3 (Skouteris et al. 2019), with this expected to be efficient in hot core environments (Taquet et al. 2016).

3.3.7. CH_2OHCHO and $(\text{CH}_2\text{OH})_2$ Emission

For both glycolaldehyde (CH_2OHCHO) and ethylene glycol ($(\text{CH}_2\text{OH})_2$), one transition is identified toward G28.2. Figures 6(a) and (b) show the moment 0 maps of these species. Emission from both species looks similar, being compact and peaking toward HMC1.

These two species are chemically related. $(\text{CH}_2\text{OH})_2$ could be produced via two successive hydrogen addition reactions with HOCH_2CHO (e.g., Rivilla et al. 2017; Mondal et al. 2021). They show similar distributions, which may indicate their similar chemical origin, i.e., sublimating together from grain mantles under similar conditions.

3.3.8. CH_3CHO Emission

Five transitions of acetaldehyde (CH_3CHO) are detected toward G28.2 (see Table 3). Among them, we have two similar sets of transitions based on their E_{up} values. The line widths of all these transitions are similar. The moment 0 map of one transition ($E_{\text{up}} = 93$ K) of CH_3CHO is depicted in Figure 6(c). It shows bright emission toward HMC1 and faint emission toward HMC2. We do not see any emission toward HMC3.

This molecule is expected to be produced on grain surfaces via radical–radical reactions between HCO and CH_3 and between H and CH_3CO (Ruaud et al. 2015; Enrique-Romero et al. 2020). It may also be produced efficiently via gas-phase reactions (Vazart et al. 2020). However, the morphological similarities with the high E_{up} transitions of CH_3OH and CH_3CHO suggest that in G28.2 it is primarily formed on grain surfaces.

3.3.9. $\text{C}_2\text{H}_5\text{OH}$ Emission

Five transitions of ethanol ($\text{C}_2\text{H}_5\text{OH}$) with different upper state energies are detected toward G28.2 (see Table 3). The moment 0 map of one high-excitation ($E_{\text{up}} = 244$ K) transition is shown in Figure 6(e). The spatial distribution of ethanol shows that its emission is peaked toward HMC1 and similar to the spatial distribution of CH_3CHO .

The morphological correlation between CH_3CHO and $\text{C}_2\text{H}_5\text{OH}$ emission indicates similar chemical origins. Ethanol can be produced via two successive hydrogen addition reactions with CH_3CHO and it can also be produced via various ion–neutral gas-phase and radical–radical reactions (e.g., Gorai et al. 2017; Mondal et al. 2021).

3.3.10. CH_3COCH_3 Emission

Two transitions with equivalent upper state energy ($E_{\text{up}} = 155$ K) of acetone (CH_3COCH_3) are detected toward our target. A moment 0 map of one of these transitions is shown in Figure 6(d). It reveals that the distribution of CH_3COCH_3 is similar to that of dimethyl ether, indicating some linkage of their formation routes.

Acetone is expected to mainly form via radical–radical recombination of methyl (CH_3O) and acetyl radical (CH_3CO) radicals on the grain surfaces (Garrod et al. 2008). Recently,

Singh et al. (2022) studied the formation of acetone and its isomers in the laboratory with an interstellar ice analog composed of methane and acetaldehyde and proposed new branching ratios of their formation. In principle, acetone could also be produced in the gas phase via molecular radiative association, such as $\text{CH}_3^+ + \text{CH}_3\text{CHO} \rightarrow (\text{CH}_3)_2\text{CHO}^+$, followed by dissociative recombination (Combes et al. 1987). However, the rates of gas-phase reactions are not expected to be as important as the surface reaction routes.

3.3.11. CH_3OCHO Emission

Methyl formate (CH_3OCHO) is commonly observed in HMCs. Two transitions of CH_3OCHO are detected toward G28.2 (see Table 3). The moment 0 map of one transition ($E_{\text{up}} = 379$ K) is shown in Figure 6(f). The distribution of CH_3OCHO emission is compact and peaks toward HMC1 and HMC2, and as with a number of other species previously discussed, is brighter toward HMC1.

Methyl formate is expected to be formed mainly via radical–radical reactions, i.e., the reaction between CH_3O and CHO radicals (e.g., Garrod & Herbst 2006). It may also be formed in the gas phase at low temperatures, including its precursor, methoxy (CH_3O) radical (Balucani et al. 2015).

3.3.12. HNCO Emission

Isocyanic acid (HNCO) is an important nitrogen-bearing molecule, which is the precursor of many prebiotic species (e.g., NH_2CHO). One transition of HNCO ($E_{\text{up}} = 470$ K) is detected toward G28.2. Figure 7(f) shows the moment 0 map of HNCO . This reveals the main emission peak toward HMC1. There is also some emission toward HMC2. The morphological emission of HNCO is similar to that of other COM species (e.g., CH_3OH , CH_3OCH_3) that are thought to be mostly produced on the grain surface and released to the gas phase via thermal processes.

3.3.13. NH_2CHO Emission

One transition ($E_{\text{up}} = 61$ K, see Table 3) of formamide (NH_2CHO) is detected toward G28.2. Figure 7(a) shows the moment 0 map of this species. The emission structure of NH_2CHO coincides with that of HNCO emission peaks. The derived column densities of NH_2CHO to HNCO (see below) are approximately 0.36. The moment 1 map of NH_2CHO is depicted in Figure A1(e). The southern part is redshifted, while the northern side is blueshifted. The velocity separation of these regions is about 2 km s^{-1} .

NH_2CHO has been proposed to be mainly produced on grain surfaces via two successive hydrogen addition reactions with HNCO (e.g., Ligterink et al. 2017; Gorai et al. 2020). NH_2CHO is also thought to be related to dual cyclic hydrogen addition and abstraction reactions Haupa et al. 2019, with this having been tested in an astrochemical model (Gorai et al. 2020). The similar morphological structures of HNCO and NH_2CHO further support the chemical link between them.

However, an alternative mechanism involves the ice-phase reaction $\text{NH}_3 + \text{CO} \rightarrow \text{NH}_2\text{CHO}$ driven by ionizing radiation (Bredehöft et al. 2017). These authors (Mues 2021, and J. H. Bredehöft, private communication) measure that this mechanism has a branching ratio of about 2:1 to alternatively produce $\text{HNCO} + \text{H}_2$. We find a column density ratio of HNCO to NH_2CHO of about 1.8 in HMC1, 2.5 in HMC2, and

$\sim 1/0.36 \simeq 2.8$ as an average of these and several other hot cores (see below) that is similar to this branching ratio, which lends support to this mechanism being at play. In addition, the spatial location of these species coincides with H30 α recombination line emission (Law et al. 2022), so the required source of ionization is likely to be present.

3.3.14. $^{13}\text{CH}_3\text{CN}$ Emission

Three transitions of the ^{13}C isotopologue of methyl cyanide ($^{13}\text{CH}_3\text{CN}$) are detected toward G28.2 (see Table 3). Moment 0 maps of two different transitions are shown in Figures 7(d) and (e). CH_3CN was previously identified toward G28.2 by Qin et al. (2008). The spatial distributions of both CH_3CN and $^{13}\text{CH}_3\text{CN}$ show similar morphologies.

3.3.15. $\text{C}_2\text{H}_3\text{CN}$ Emission

Vinyl cyanide ($\text{C}_2\text{H}_3\text{CN}$) has significant importance in prebiotic chemistry, in particular by its ability to form branched chain molecules and amino acids (e.g., Garrod et al. 2017). Five transitions of vinyl cyanide are identified toward G28.2 (see Table 3). The moment 0 map of one ($E_{\text{up}} = 145$ K) of these transitions is depicted in Figure 7(b). It shows an emission peak in the northern dense gas blob and further extends along the axis of the outflow direction, which suggests that the formation of $\text{C}_2\text{H}_3\text{CN}$ may be influenced by shocks in the outflowing gas. It also shows emission peaks similar to other COMs, i.e., toward HMC1.

The $\text{C}_2\text{H}_2\text{CN}$ radical is expected to form on the grain surface via either a reaction between H and HC_3N or a reaction between CN and C_2H_2 (Garrod et al. 2017). However, both reactions have activation barriers, 1710 K and 1300 K, respectively. Thereafter one hydrogen addition reaction with the $\text{C}_2\text{H}_2\text{CN}$ radical produces $\text{C}_2\text{H}_3\text{CN}$. At about 40–50 K, $\text{C}_2\text{H}_3\text{CN}$ could be produced in the gas phase through C_2H_4 and CN (Garrod et al. 2017). The temperatures in both HMC1 and in shocked regions are likely to be sufficient to overcome the activation barrier of this reaction. This may explain why we see peak emissions of $\text{C}_2\text{H}_3\text{CN}$ toward both HMC1 and in the outflowing shock gas near HMC3 (see Figure 7). The relative faintness of $\text{C}_2\text{H}_3\text{CN}$ toward HMC1 compared to HMC3 is potentially due to reactions occurring efficiently at HMC1 so that much of the $\text{C}_2\text{H}_3\text{CN}$ is already converted to $\text{C}_2\text{H}_5\text{CN}$ due to the higher temperatures there (~ 300 K).

3.3.16. $\text{C}_2\text{H}_5\text{CN}$ Emission

In the case of ethyl cyanide ($\text{C}_2\text{H}_5\text{CN}$), four transitions are detected toward G28.2. In addition to the main species, three transitions of the ^{13}C isotopologue of $\text{C}_2\text{H}_5\text{CN}$ are also identified (Table 3). Moment 0 and 1 maps of $\text{C}_2\text{H}_5\text{CN}$ are shown in Figure 7 and Figure A1, respectively. Figure 7(c) shows that $\text{C}_2\text{H}_5\text{CN}$ has four distinct emission peaks, i.e., in addition to HMC1, HMC2, and HMC3 there is a fourth peak at the eastern edge of the ring.

$\text{C}_2\text{H}_5\text{CN}$ formation is directly related to $\text{C}_2\text{H}_3\text{CN}$ via two successive hydrogen addition reactions on the surfaces of grains (e.g., Garrod et al. 2017). The first reaction has an activation barrier of (619–1320 K), while the second reaction is barrier-less. As discussed in the previous section, this could be the reason why $\text{C}_2\text{H}_5\text{CN}$ is very bright and $\text{C}_2\text{H}_3\text{CN}$ is less bright toward HMC1 and vice versa for HMC3 and in the outflowing gas. This could be due to the lower temperature in

the northern regions away from HMC1. We note that this species may also be formed efficiently via radical–radical reactions between CH_3 and CH_2CN (Garrod et al. 2017).

3.4. Core Temperatures from Line Spectra

Here, we use the strength of certain observed lines in the spectra of HMC1, HMC2, and HMC3 to constrain their gas temperatures. We calculate synthetic spectra using local thermodynamic equilibrium (LTE) modeling with CASSIS. For such modeling, we used five adjustable parameters: (i) column density; (ii) excitation temperature (T_{ex}); (iii) line width (Δv); (iv) velocity (v_{LSR}); and (v) source size (θ_s). Here, we focus on the effects of varying T_{ex} to find reasonable values for the HMCs.

Figure 8 shows an example of synthetic spectra compared with observed spectra for HMC1 and HMC2. Here, we choose three high-excitation transitions of three different species: HNCO ($E_{\text{up}} = 470$ K); CH_3OCHO ($E_{\text{up}} = 379$ K); and $^{13}\text{CH}_3\text{CN}$ ($E_{\text{up}} = 335$ K). For HMC1, we find that a fiducial temperature of $T_{\text{ex}} = 100$ K is unable to reproduce the observed line profiles of these three species; instead, we need a higher temperature, ~ 300 K, to do so. Similarly, for HMC2, we need a temperature of ~ 250 K. However, for HMC3, which lacks detections of the above high-excitation transitions, we find $T_{\text{ex}} = 70$ K is a suitable temperature to reproduce the observed spectral lines.

Thus, when we evaluate column densities and abundances of species for the HMCs, we will present results for each core where T_{ex} is set to 300, 270, and 70 K for HMC1, HMC2, and HMC3, respectively. We view this case as being more accurate. Physically, we also identify these fitted T_{ex} values as being reasonable estimates for the average gas temperatures of the HMCs. Given the high densities, we expect the dust temperature to be well coupled to the gas temperature. We have thus used these temperatures for our fiducial mass surface density estimates in Section 3.1.

3.5. Column Densities of the Observed Species

To estimate the column densities of the observed species, we use the same CASSIS modeling as in Section 3.4, but now with a focus on constraining the column density of each species. We present results using the individually constrained temperatures of each core from Section 3.4. Note that the value of N_{H} has a dependence on the assumed temperature, given the results of Section 3.1, which thus also affects absolute abundance estimates. The values used for line widths in the modeling are set by the observed values given in Table 3. Then the column density of each species was varied to obtain a best fit to the observed spectra. Comparisons of observed and synthetic spectra for HMC1, HMC2, and HMC3 are shown in Figures B1–B3, respectively.

The derived column density of each species (N_{X}) and its abundance with respect to H ($N_{\text{X}}/N_{\text{H}}$) are listed in Tables 4 and 5 for every species detected in each of HMC1, HMC2, and HMC3. Here, we also list literature results for three additional HMCs: Orion KL, G10.47, and G328.2. Figure 9 presents a visual representation of these data. Correlations between certain species that hint at chemical linkage are discussed below in Section 4.

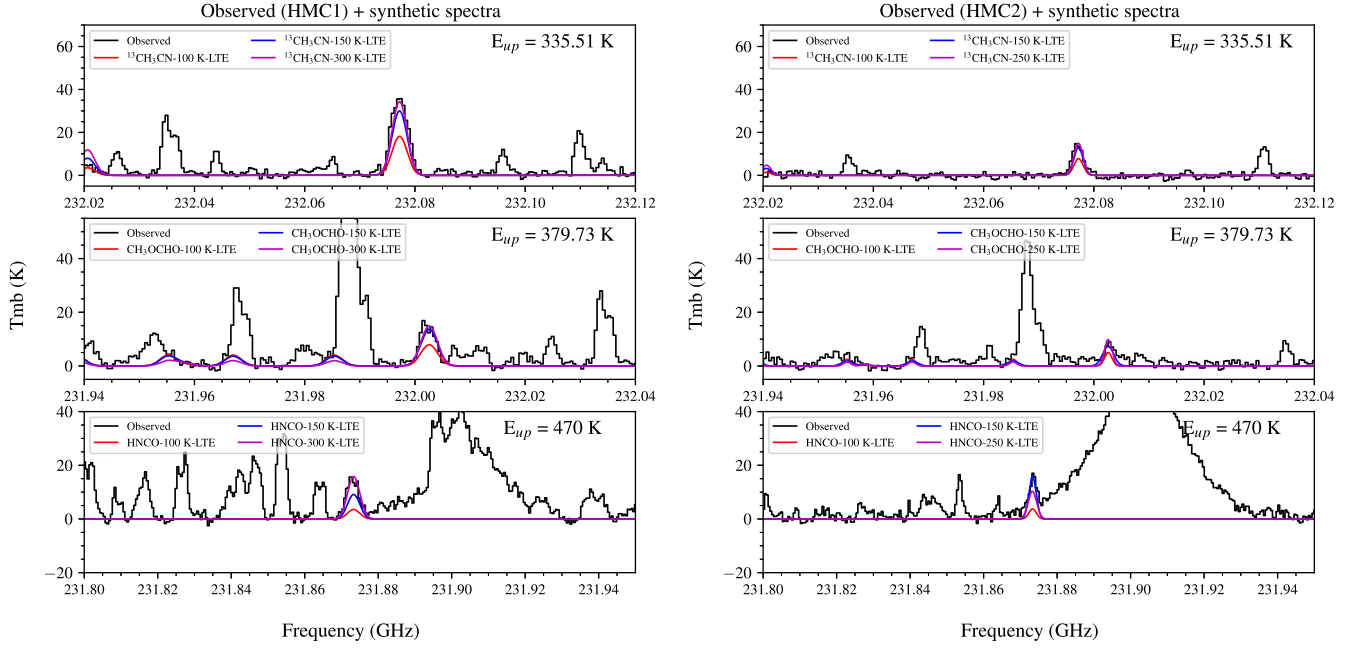


Figure 8. (a) Left panel: comparison between observed and synthetic spectra for HMC1, where black lines are observed spectra and red, blue, and magenta lines are synthetic spectra at 100, 150, and 300 K, respectively. (b) Right panel: as in (a), but for HMC2 and with synthetic spectra now shown for 100, 150, and 250 K.

Table 4
Comparison of Observed Molecular Column Densities between G28.2 and Other Sources

Species	G28.2 HMC1 Column Density (cm ⁻²)	G28.2 HMC2 Column Density (cm ⁻²)	G28.2 HMC3 Column Density (cm ⁻²)	Orion KL (HMC) Column Density (cm ⁻²)	G10.47+0.03 Column Density (cm ⁻²)	G328.2 Column Density (cm ⁻²)
N _H	1.98×10^{24}	2.58×10^{24}	6.55×10^{24}	4.0×10^{24}	1.0×10^{25}	3.8×10^{24}
SO ₂	8.40E+16	7.65E+16	1.50E+17	4.16E+17	3.00E+17	1.60E+17
H ₂ S	5.00E+16	1.50E+16	2.00E+16	1.70E+17	4.10E+16	4.80E+16
H ₂ CO	3.50E+17	1.30E+17	8.00E+16	3.20E+17	3.00E+18	4.15E+15
CH ₃ OH	1.33E+19	2.21E+18	9.00E+16	3.20E+18	9.00E+18	4.10E+18
CH ₃ CHO	5.95E+16	2.45E+16	1.00E+15	6.99E+15	1.95E+14	6.83E+15
C ₂ H ₅ OH	4.50E+17	5.00E+16	...	7.56E+15	6.00E+17	9.00E+16
HNCO	3.15E+16	2.50E+16	...	1.19E+16	1.30E+17	2.70E+16
NH ₂ CHO	1.75E+16	1.00E+16	...	4.00E+15	3.80E+16	4.20E+16
C ₂ H ₃ CN	7.00E+15	4.00E+15	1.00E+15	2.91E+15	7.00E+17	2.00E+16
C ₂ H ₅ CN	2.00E+16	4.60E+15	2.00E+15	1.15E+16	9.00E+17	4.80E+16
¹³ CH ₃ CN	6.00E+15	1.50E+15
CH ₃ OCH ₃	9.00E+17	6.00E+16	1.20E+16	1.59E+17	1.50E+18	2.10E+18
CH ₃ COCH ₃	3.50E+17	6.00E+16	...	5.43E+15	5.40E+17	4.10E+16
CH ₃ OCHO	4.50E+17	1.00E+17	...	2.69E+16	9.10E+17	1.00E+17
CH ₂ OHCHO	4.20E+16	1.20E+16	...	3.50E+14	1.30E+16	—
(CH ₂ OH) ₂	1.20E+16	1.40E+15	...	4.60E+15	5.00E+17	4.00E+16

Note. Orion KL (HMC) (Feng et al. 2015) $T_{\text{ex}} \sim 130\text{--}200$ K, resolution $3''0 \sim 1220$ au; (Mangum et al. 1988) $T_{\text{ex}} \sim 250$ K, resolution $6''0 \sim 2500$ au; (Cernicharo et al. 2016) $T_{\text{ex}} \sim 200$ K, resolution $9''0 \sim 3700$ au; (Luo et al. 2019) $T_{\text{ex}} \sim 176$ K, resolution $1''4 \sim 580$ au; (Brouillet et al. 2015) $T_{\text{ex}} \sim 145$ K, resolution $1''3 \sim 500$ au, G10.47; (Rolffs et al. 2011) $T_{\text{ex}} \sim 200$ K, resolution $0''35 \sim 3700$ au; (Gorai et al. 2020; Mondal et al. 2021) $T_{\text{ex}} \sim 200$ K, resolution $2''0 \sim 21,000$ au, G328.2; (Csengeri et al. 2019) $T_{\text{ex}} \sim 110$ K, resolution $0''23 \sim 575$ au; (Bouscasse et al. 2022) $T_{\text{ex}} \sim 130\text{--}170$ K, resolution $14''\text{--}36''$.

4. Discussion

4.1. Nature of HMCs

We have found three HMCs, defined by the average locations of peak intensities of line emission from COMs and other species. The HMCs have properties derived from apertures of $0''15$ radius, i.e., 850 au. These HMCs are located in and around the millimeter continuum ring of the G28.2 massive protostar. HMC1 is the closest, in projection, to the massive protostar; indeed, its area overlaps with this position. It

is also the most chemically rich and warmest (~ 300 K). HMC2 is about 2000 au away in projection, of intermediate chemical complexity, and slightly cooler (~ 250 K) than HMC1. HMC3 is about 3000 au away in projection, shows the fewest lines in its spectrum, and is the coolest (~ 70 K). All the HMCs have typical $\Sigma_{1.3\text{mm}} \sim 10$ g cm⁻² and thus masses of ~ 1 to $\sim 4 M_{\odot}$ (note that HMC3 is inferred to be the most massive).

By investigating the spatial offset of line emission peaks from the main millimeter continuum source as a function of upper-state energy, we have found evidence for a gradient of

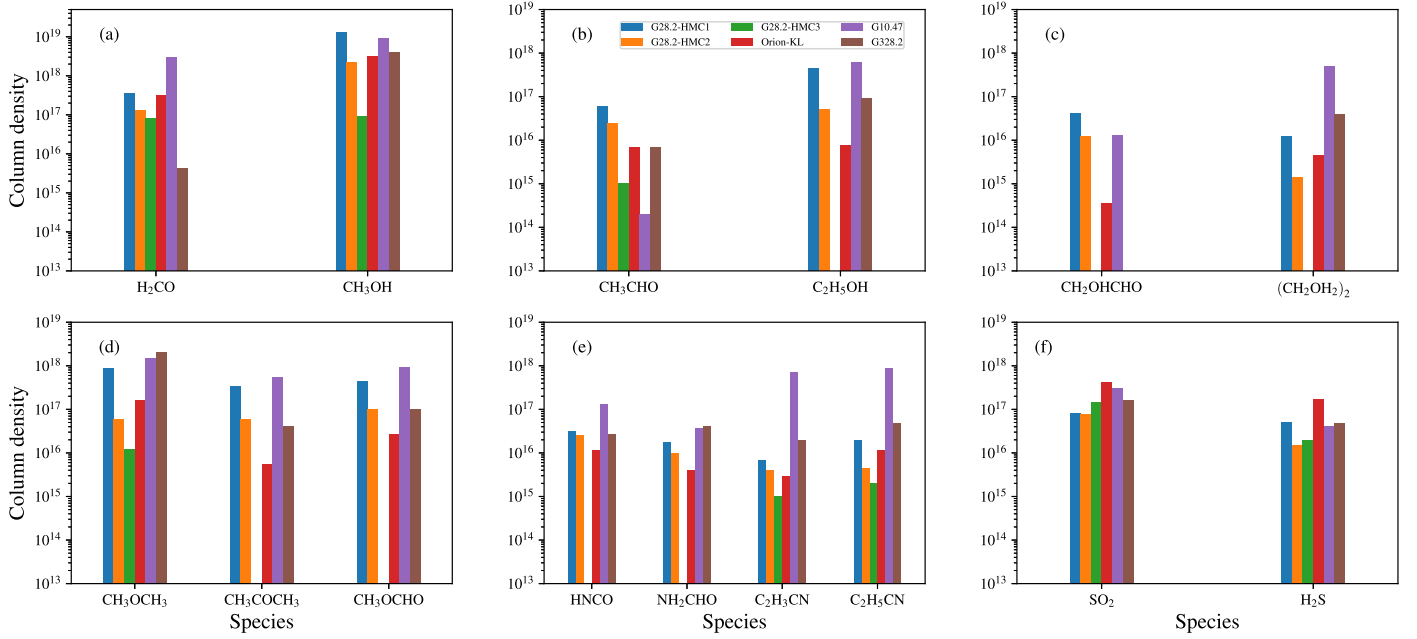


Figure 9. Column densities of various observed molecules toward HMC1, HMC2, and HMC3 in G28.2, and their comparison with the equivalent results for HMCs Orion KL, G10.47, and G328.2. The first four panels (a)–(d) show oxygen-bearing molecules. Panel (e) shows nitrogen-bearing species, while panel (f) shows sulfur-bearing species. (a) Column densities of H_2CO and CH_3OH . (b) Column densities of CH_3CHO and $\text{C}_2\text{H}_5\text{OH}$. (c) Column densities of CH_2OHCHO and $(\text{CH}_2\text{OH})_2$. (d) Column densities of CH_3OCHO , CH_3OCH_3 , and CH_3COCH_3 . (e) Column densities of HNCO , NH_2CHO , $\text{C}_2\text{H}_3\text{CN}$, and $\text{C}_2\text{H}_5\text{CN}$. (f) Column densities of SO_2 and H_2S .

Table 5
Comparison of Observed Molecular Abundances w.r.t H Nuclei between G28.2 and Other Sources

Species	G28.2 HMC1 Abundance	G28.2 HMC2 Abundance	G28.2 HMC3 Abundance	Orion KL (HMC) Abundance	G10.47+0.03 Abundance	G328.2 Abundance
SO_2	4.24E-08	2.97E-08	2.29E-08	1.04E-07	3.00E-08	4.21E-08
H_2S	2.53E-08	5.81E-09	3.05E-09	4.25E-08	4.10E-09	1.26E-08
H_2CO	1.77E-07	5.04E-08	1.22E-08	8.00E-08	3.00E-07	1.09E-09
CH_3OH	6.71E-06	8.57E-07	1.37E-08	8.00E-07	9.00E-07	1.08E-06
CH_3CHO	3.01E-08	9.50E-09	1.53E-10	1.75E-09	1.95E-11	1.80E-09
$\text{C}_2\text{H}_5\text{OH}$	2.27E-07	1.94E-08	...	1.89E-09	6.00E-08	2.37E-08
HNCO	1.59E-08	9.69E-09	...	2.98E-09	1.30E-08	7.11E-09
NH_2CHO	8.84E-09	3.88E-09	...	1.00E-09	3.80E-09	1.11E-08
$\text{C}_2\text{H}_3\text{CN}$	3.54E-09	1.55E-09	1.53E-10	7.25E-10	7.00E-08	5.26E-09
$\text{C}_2\text{H}_5\text{CN}$	1.01E-08	1.78E-09	3.05E-10	2.88E-09	9.00E-08	1.26E-08
$^{13}\text{CH}_3\text{CN}$	3.03E-09	5.81E-10
CH_3OCH_3	4.55E-07	2.33E-08	1.83E-09	3.98E-08	1.50E-07	5.53E-07
CH_3COCH_3	1.77E-07	2.33E-08	...	1.36E-09	5.40E-08	1.08E-08
CH_3OCHO	2.27E-07	3.88E-08	...	6.73E-09	9.10E-08	2.63E-08
CH_2OHCHO	2.12E-08	4.65E-09	...	8.75E-11	1.30E-09	...
$(\text{CH}_2\text{OH})_2$	6.06E-09	5.43E-10	...	1.15E-09	5.00E-08	1.05E-08

Note. Orion KL (HMC) (Feng et al. 2015) $T_{\text{ex}} \sim 130\text{--}200$ K, resolution $3''0 \sim 1220$ au; (Mangum et al. 1988; Cernicharo et al. 2016) $T_{\text{ex}} \sim 200$ K, resolution $9''0 \sim 3700$ au; (Luo et al. 2019) $T_{\text{ex}} \sim 176$ K, resolution $1''4 \sim 580$ au; (Brouillet et al. 2015) $T_{\text{ex}} \sim 145$ K, resolution $1\text{v}3 \sim 500$ au, G10.47; (Rolfs et al. 2011) $T_{\text{ex}} \sim 200$ K, resolution $0''35 \sim 3700$ au; (Gorai et al. 2020; Mondal et al. 2021) $T_{\text{ex}} \sim 200$ K, resolution $2''0 \sim 21,000$ au, G328.2; (Csengeri et al. 2019) $T_{\text{ex}} \sim 110$ K, resolution $0''23 \sim 575$ au; (Bouscasse et al. 2022) $T_{\text{ex}} \sim 130\text{--}170$ K, resolution $14''\text{--}36''$.

temperature along vectors that point away from the massive protostar (see Figure 2). This analysis indicates that HMC1, HMC2, and HMC3 are not internally heated, i.e., all the HMCs are spatially displaced from the massive protostar. These observations also confirm that there is dense molecular gas present at all locations around the millimeter continuum ring.

The above results indicate the presence of significant amounts of dense, warm, clumpy molecular gas within a few thousand astronomical units of a massive protostar. The total mass of HMC1, HMC2, and HMC3 is about $7 M_{\odot}$. Law et al.

(2022) estimated a total gas mass within a $0''5$ (~ 3000 au) radius of about $30 M_{\odot}$, assuming, as we have done for HMC1 and HMC2, that half the total flux is due to free-free emission and for a constant temperature of $T_d = 100$ K. Using a value of 200 K would lower this estimate to $15 M_{\odot}$. In comparison, our results that infer a temperature gradient from ~ 300 K for HMC1 to ~ 70 K for HMC3 imply lower gas masses in the inner region of the millimeter continuum ring, but larger masses in the regions just outside of it. Given the fractional areal coverage we have included in the definition of the HMCs,

we estimate that the total gas mass within a region of ~ 3000 au is about 3.7 times larger than that of the total of the cores, i.e., $\sim 25 M_{\odot}$. This mass is comparable to that estimated for the current protostellar mass, i.e., $m_{*} \sim 40 M_{\odot}$ (Law et al. 2022). The existence of this material on these scales is an important constraint for theoretical models and simulations of massive star formation.

The molecular gas may either be in the process of infall to join the protostar, likely via an accretion disk or is in the process of being swept up by the mechanical and/or radiative feedback from the star. Since there is clear evidence that the protostar is driving powerful bipolar outflows (Law et al. 2022), we favor an interpretation that at least some of the hot core material is still in the infall phase. In this case, the observations indicate that gas is quite structured within the infall envelope. Such structure, including infalling streamers that can show significant curvature, is a natural expectation of the turbulent core accretion model of massive star formation (McKee & Tan 2003), e.g., as seen in the simulations of Myers et al. (2013). However, these authors, who simulated a $300 M_{\odot}$ core with an initial radius of 0.1 pc and initial magnetic field strength of 1.6 mG, did not see mass surface densities greater than $\sim 3 \text{ g cm}^{-2}$ within the inner ~ 3000 au region, at least to the point when the protostar had grown to $16 M_{\odot}$ (see also Figure 4 of Tan et al. 2014). Nevertheless, higher mass surface densities may arise either at later evolutionary stages or for cores that start from an initially denser state, i.e., higher surrounding clump mass surface density.

Infall streamers to massive protostars have been previously detected and modeled, e.g., in the case of IRAS 07299-1651 (Zhang et al. 2019). In this case, the kinematics of an infalling streamer, as traced by CH_3OH , could be modeled with a simple ballistic infall solution. The kinematics of the inner region of G28.2, including its millimeter continuum ring, appear more complex (see, e.g., Figure A1) and it remains uncertain whether the motions of the ring material are shaped more by infall or outflow, with the latter potentially induced by protostellar outflow, ionization, or radiation pressure feedback. In particular, since $\text{H}30\alpha$ emission is detected all around the millimeter continuum ring (Law et al. 2022), ionization feedback is likely to play an important role in this environment.

In terms of evidence for rotation in the molecular gas, we do not see very clear evidence for velocity gradients that are perpendicular to the outflow axis and that match the pattern of the $\text{H}30\alpha$ velocity gradient reported by Law et al. (2022) from the analysis of the long baseline data (i.e., blueshifted to the SE and redshifted to NW of the main millimeter continuum peak). The $\text{H}30\alpha$ emission may be tracing the rotating surface of an ionized disk wind, which extends to larger scales than the rotating infall envelope. In general, fully rotationally supported disk structures are expected to be present on smaller scales, $\lesssim 100$ au (e.g., Myers et al. 2013), which would not be resolved by the data we have analyzed, i.e., with a beam of $0''.2$ equivalent to ~ 1000 au.

4.2. Comparison of Column Densities of Different Species

We use our measured column densities in G28.2 HMC1, HMC2, and HMC3, and in three other HMCs that have similar spatial scales (Orion KL—hot core; G10.47; G328.2) to explore potential correlations and abundance ratios between chemically related species. These results provide constraints for

astrochemical models of hot cores. Figure 10 shows some of our explored correlations.

The measured column density and abundance of CH_3OH , as determined from its line profile, may be subject to potential underestimation due to high line opacity (see Figure 3). To mitigate this issue, we have measured abundances from the rarer species $^{13}\text{CH}_3\text{OH}$. For this, we measure the column density of $^{13}\text{CH}_3\text{OH}$ and then use an estimated $^{12}\text{C}/^{13}\text{C}$ ratio to derive the column density of CH_3OH . The $^{12}\text{C}/^{13}\text{C}$ isotopologue ratio is estimated to be 44.2 using the relation of Milam et al. (2005) and setting the Galactocentric distance of the source to be 4.11 kpc. The column densities of $^{13}\text{CH}_3\text{OH}$ are measured as $3 \times 10^{17} \text{ cm}^{-2}$ toward HMC1 and $5 \times 10^{16} \text{ cm}^{-2}$ toward HMC2.

A clear correlation is observed for H_2CO and CH_3OH (Figure 10(a)). These two species are chemically linked (see Section 3.3.3) and the CH_3OH column density is always higher (on average by a factor of 3.5) compared to its precursor, H_2CO . $\text{C}_2\text{H}_5\text{OH}$ and CH_3CHO also show some correlation, except for the source G10.47 (Figure 10(b)). $(\text{CH}_2\text{OH})_2$ and CH_2OHCHO show a more scattered relation (Figure 10(c)). CH_3OCH_3 and CH_3OH show a clear correlation (with the latter more abundant by an average factor of 8.3), which could be due to the fact that they are produced efficiently from the same precursor, CH_3O . The peptide bond containing species HNCO and NH_2CHO are directly linked via their formation pathways (see Section 3.3.13) and we see a clear linear correlation between them, such that the abundance of NH_2CHO is on average about 0.36 times that of HNCO (see Figure 10(h)). Finally, a near one-to-one relation is observed between $\text{C}_2\text{H}_5\text{CN}$ and $\text{C}_2\text{H}_3\text{CN}$, which are precursors of branched chain molecules (Belloche et al. 2017), with the abundance of the former about 1.3 times the latter on average.

4.3. Comparison between N-bearing and O-bearing COMs

Both O- and N-bearing species are well-known tracers of HMCs (e.g., Blake et al. 1987; Belloche et al. 2014, 2017; Rivilla et al. 2017; Gorai et al. 2021). Blake et al. (1987) observed various N- and O-bearing molecules in Orion KL with different radial velocities and found N-bearing species are enhanced in the Orion hot core and O-bearing molecules in the compact ridge. Later, astrochemical modeling results showed that such chemical differences could arise due to different physical conditions and/or evolutionary stage (e.g., Charnley et al. 1992; Caselli et al. 1993). To investigate whether the observed chemical differentiation between O- and N-bearing molecules is a general property of HMC or not, Fontani et al. 2007 studied N and O-bearing molecules in several HMCs. Similar to our results in Section 4.2, they found $\text{C}_2\text{H}_3\text{CN}$ and $\text{C}_2\text{H}_5\text{CN}$ are strongly correlated. Later, results of interferometric observations suggested O-bearing species are enhanced in the Orion compact ridge and N-bearing species are rich in the Orion hot core (e.g., Friedel & Snyder 2008; Peng et al. 2013; Feng et al. 2015), which further supported the previous results of Blake et al. (1987). Suzuki et al. (2018) studied various N- and O-bearing species in several HMCs using NRO 45 m single dish data. They did not find any correlation between N- and O-bearing species, instead finding a correlation between N-bearing molecules with other N-bearing molecules.

In G28.2 we find correlations of the spatial distributions between some of the O- and N-bearing molecules. Emission from all the detected high-excitation transitions of O-bearing

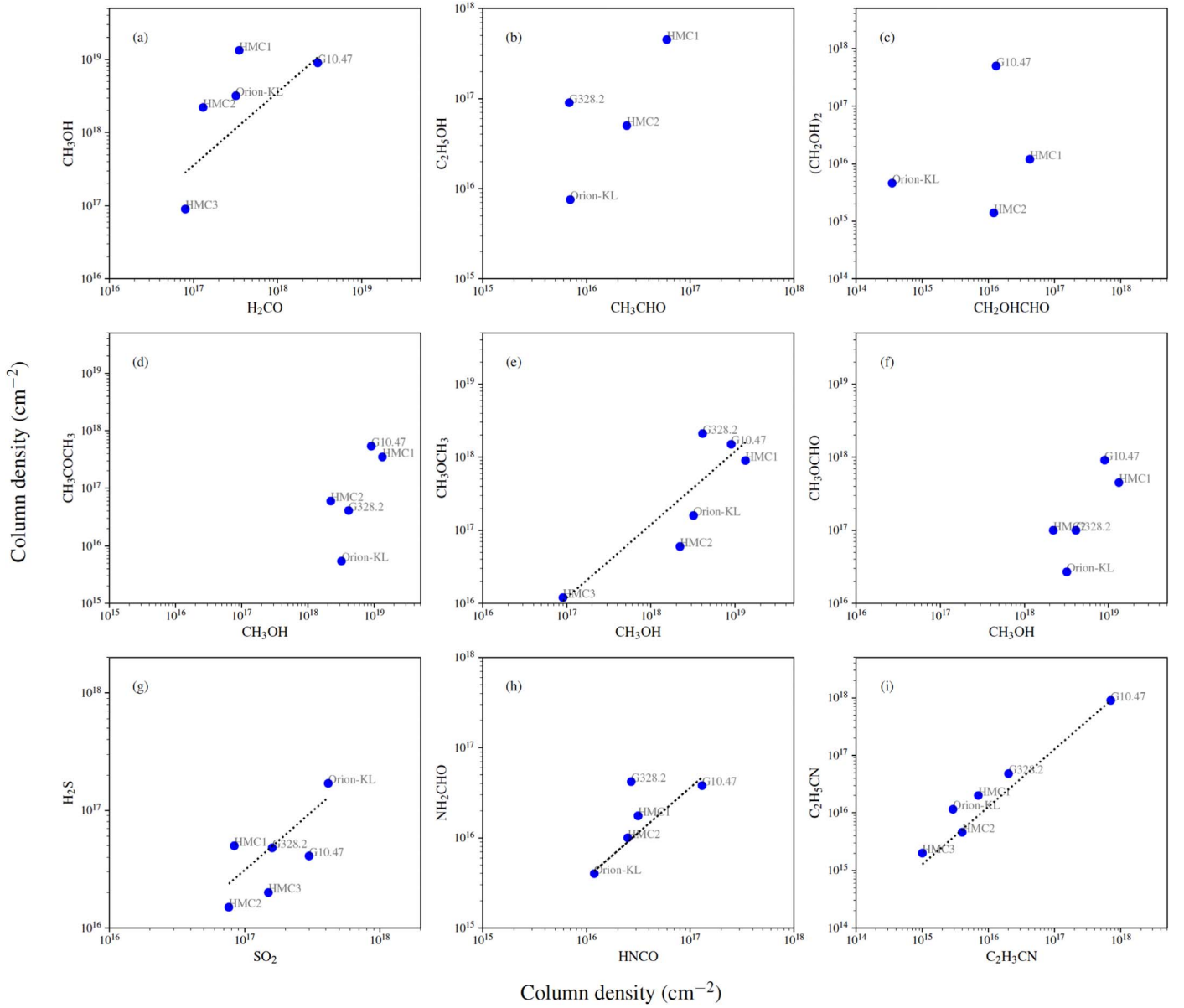


Figure 10. Correlations between column densities of different pairs of molecules in the G28.2 HMCs and three other HMCs, providing information on abundance ratios. (a) CH_3OH vs. H_2CO , with an average abundance ratio of 3.57. (b) $\text{C}_2\text{H}_5\text{OH}$ vs. CH_3CHO . (c) $(\text{CH}_2\text{OH})_2$ vs. CH_2OHCHO . (d) CH_3COCH_3 vs. CH_3OH . (e) CH_3OCH_3 vs. CH_3OH , with an average abundance ratio of 0.12. (f) CH_3OCHO vs. CH_3OH . (g) H_2S vs. SO_2 , with an average abundance ratio of 0.31. (h) NH_2CHO vs. HNCO , with an average abundance ratio of 0.36. (i) $\text{C}_2\text{H}_5\text{CN}$ vs. $\text{C}_2\text{H}_3\text{CN}$, with an average abundance ratio of 1.28.

and N-bearing COMs is compact and bright toward HMC1 and HMC2, except for $\text{C}_2\text{H}_3\text{CN}$. This suggests that O- and N-bearing COMs show similar morphological structures and are bright toward HMC1, indicating active sites of formation of both types of species. In conclusion, O- and N-bearing molecules show similar distribution hints of similar chemical origins, i.e., formation on the grains followed by sublimation into the gas phase. However, it is possible that higher angular resolution observations with the sensitivity to detect the species will reveal spatial variations on scales smaller than $\sim 0''.2$, i.e., ~ 1000 au.

4.4. Shock-induced Chemistry

In addition to the emission from HMC1, HMC2, and HMC3 in and around the continuum ring, there is also some emission

from molecular gas, including COMs, from more extended regions, especially to the NE in the direction of the known blueshifted outflow. In the inner regions of this source, SiO emission is primarily tracing outflow activity. Interestingly, as shown in Figure 11, SiO is also seen at the positions of all the HMCs, in particular with local peaks seen toward HMC1 and HMC3. Therefore, in addition to the energy from radiative heating, the molecular gas around the protostar may also be receiving significant heating from outflow-driven shocks.

It is well known that H_2CO and CH_3OH are mainly produced in grain mantles in the ice phase and then later evaporated to the gas phase. In addition to emission from hot core regions, these two species have also been observed in several outflows, with abundance enhanced by a factor of ~ 100 (e.g., Bachiller et al. 2001; Garay et al. 2002; Jørgensen et al. 2004; Maret et al. 2005) compared to the hot core region. In

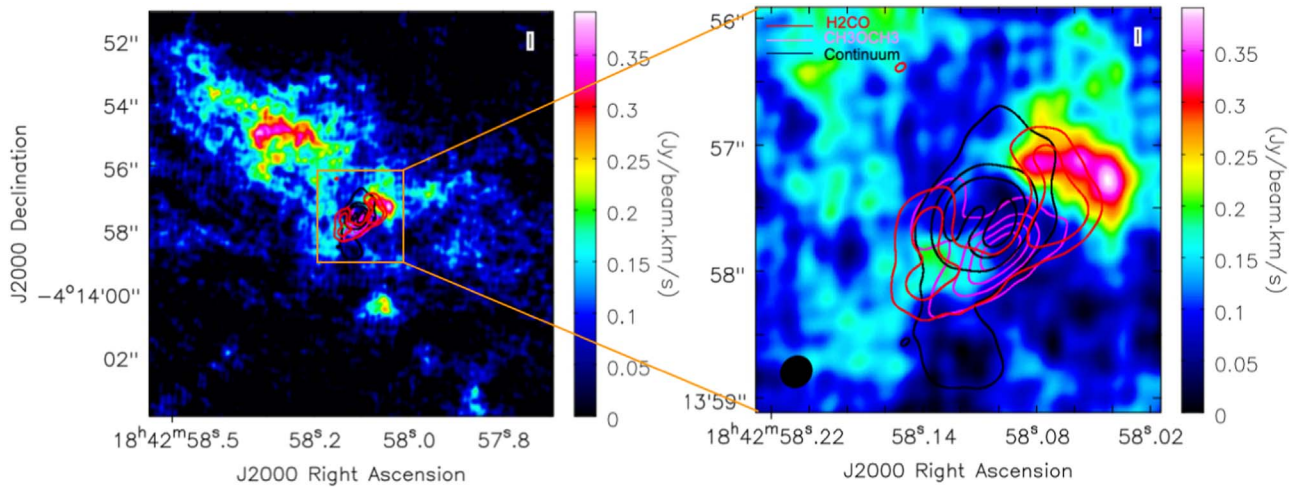


Figure 11. The color image represents the SiO emission, which mainly traces shocks. Red and magenta contours represent high-excitation H_2CO and CH_3OCH_3 , respectively. The black contour represents the continuum contours.

particular, low-excitation transitions of H_2CO and CH_3OH have been found to be good tracers of outflow shocks (e.g., Arce et al. 2007; Taniguchi et al. 2020; Zhang et al. 2021).

In G28.2, we find some morphological similarity of the low-excitation H_2CO and CH_3OH transitions with the SiO emission. Thus, it is evident that in the extended regions, the main reason for the enhancement of H_2CO and CH_3OH is due to the presence of shocks. On the other hand, we also see extended emission of H_2S , whose enhanced emission peak overlaps the SiO emission peak (see Section 4.5 for further discussion).

4.5. Sulfur-bearing Species

In diffuse clouds, observed abundances of sulfur reflect the elemental abundance ($\sim 10^{-5}$) (e.g., Savage & Sembach 1996; Howk et al. 2006). However, the main reservoir of sulfur is still puzzling (e.g., Tieftrunk et al. 1994; Woods et al. 2015). In dense molecular clouds, S-bearing molecules are thought to be depleted onto grain surfaces, which could be the main reason why the observed gas-phase abundance of sulfur does not reflect its cosmic elemental abundance. It remains a long-standing open question as to which species are the main S-bearing species in these environments. So far, only two S-bearing species have been identified on grain surfaces: OCS and SO_2 (Palumbo et al. 1995; Boogert et al. 1997; Palumbo et al. 1997). However, the abundance of SO_2 is not thought to make a major contribution to the S reservoir. Instead, based on various observational and especially modeling results, H_2S and OCS have been thought to be the most important S-bearing species. (e.g., Charnley 1997; Wakelam et al. 2004; Podio et al. 2014).

Previously, two S-bearing molecules, SO_2 ($J'_{K'aK'c} - J''_{K''aK''c} = 11,1,11 - 10,0,10$) and OCS ($J'_{K'aK'c} - J''_{K''aK''c} = 19-18$) were detected toward G28.2 (Qin et al. 2008; Klaassen et al. 2009). Klaassen et al. (2009) analyzed Submillimeter Array data and studied moment maps of SO_2 and OCS. They found different distributions of emissions for these two species (see their Figure 2). They concluded that these molecules trace gas surrounding the H II region, which appears to be rotating. They also noticed different velocity gradients for these two species. However, these features were only marginally resolved by their observations (i.e., a beam of $1''$ – $5700''$ au). Our

observations have ~ 5 times higher angular resolution (i.e., a beam of $0''.22$ – $1250''$ au). We have detected and spatially resolved three S-bearing molecules: ^{18}OCS ; SO_2 ; and H_2S (see Table 3). Among these, H_2S and ^{18}OCS are the first detections in this source, while the high-excitation transition of SO_2 is also a new detection. These three S-bearing species show very different spatial distributions, indicating that they trace different physical environments and that they most likely have different chemical origins.

Figure 5(d) shows SO_2 ($E_{\text{up}} = 248$ K) emission, which traces the millimeter continuum ring in the inner regions of the protostellar core. Figure A1(b) shows that this gas has complex kinematics, with the velocity centroid varying by several kilometers per second at different locations around the ring.

Our ^{18}OCS emission shows a distribution similar to that of OCS (see Figure 2, Klaassen et al. 2009), which itself is similar to other COMs seen in this source such as methanol, acetaldehyde, and dimethyl ether. Similar distributions of these species may indicate a similar origin, i.e., on grain surfaces and then sublimated to the gas phase. H_2S and OCS are thought to be the major reservoirs of sulfur, which might have been locked onto the grain surface (Charnley 1997; Wakelam et al. 2004; Podio et al. 2014). We see a completely different distribution of H_2S (see Figure 4(d)) as compared to OCS and other COMs, indicating different formation paths, i.e., H_2S may have been produced in the gas phase rather than on grain surfaces. Some morphological similarities between emission peaks of SiO and H_2S suggest that H_2S also traces shocks in the outflowing gas.

5. Conclusions

We have analyzed high angular resolution ($\sim 0''.2$) ALMA 1.3 mm (Band 6) data of G28.2, an isolated massive protostar, to study the astrochemical inventory and characterize conditions in the dense molecular gas that is forming the star. The main results are as follows:

1. Based on an investigation of spectra and emission maps of different observed species, we identify three main HMCs, HMC1, HMC2, and HMC3, in the immediate vicinity (within ~ 3000 au in projection) of the massive protostar. HMC1 and HMC2 are part of the previously identified millimeter continuum ring-like structure, while

- HMC3 is slightly further away. These cores are estimated to have temperatures of 300, 250, and 70 K, respectively, have mass surface densities of $\sim 10 \text{ g cm}^{-2}$, densities $n_{\text{H}} \sim 10^9 \text{ cm}^{-3}$, and masses from ~ 1 to $\sim 4 M_{\odot}$. The total mass of molecular gas within 3000 au is estimated to be $\sim 25 M_{\odot}$, which is similar to that of the central protostar ($m_{*} \sim 40 M_{\odot}$) and this provides an important constraint on theoretical models of massive star formation.
2. There is evidence for a systematic increase in the offset of line emission from the main continuum peak with decreasing upper state energy of the transition. This is tentative evidence of temperature gradients in the cores, indicating that they are heated externally by the central protostar. The presence of outflow tracers (SiO and high-velocity CO) in the region also indicates a possibility of shock heating in and around the cores. Our high spatial resolution also allows us to see the detailed morphologies of high-excitation species and larger COMs concentrated in the inner region, in and around the millimeter continuum ring, and the presence of lower excitation emission from relatively simple species in the more extended, $\sim 0.1 \text{ pc}$ scale core envelope. There is also evidence for larger-scale outflow shocks enhancing certain species, including H_2S and low-excitation transitions of H_2CO and CH_3OH , in the extended region.
 3. HMC1 is the most chemically rich, followed by HMC2 and then HMC3. Overall eight simple species and 14 COMs have been identified, making this source relatively chemically rich compared to other massive protostars that have been observed with the same type of ALMA observation.
 4. Assuming LTE and optically thin conditions, we have estimated the column densities of all the observed species by comparison with synthetic spectra. We have thus estimated absolute abundances and abundance ratios that provide useful constraints for astrochemical models of hot cores. Including data for an additional three other HMCs from the literature, we find evidence for correlations between column densities of certain pairs of species, i.e., approximately constant abundance ratios, which is evidence for their formation in linked astrochemical processes. These pairs include CH_3OH versus H_2CO , with an average abundance ratio of 3.57; CH_3OCH_3 versus CH_3OH , with an average abundance ratio of 0.12; H_2S versus SO_2 , with an average abundance ratio of 0.31; NH_2CHO versus HNCO , with an average abundance

ratio of 0.36; and $\text{C}_2\text{H}_5\text{CN}$ versus $\text{C}_2\text{H}_3\text{CN}$, with average abundance ratio of 1.28.

5. Various sulfur-bearing exhibit a variety of morphological structures in G28.2. OCS has a morphology concentrated toward the central millimeter continuum ring, including HMC1 and HMC2, which is similar to many of the COM species, indicating an origin in the evaporation of grain mantles. SO_2 , seen via a single high-excitation transition, is also concentrated in and around the millimeter continuum ring. However, H_2S shows much more extended emission, similar to that of H_2CO and CH_3OH , on scales of $\sim 0.1 \text{ pc}$ and likely influenced by protostellar outflow shocks.

Acknowledgments

This paper makes use of the following ALMA data: ADS/JAO.ALMA#2016.1.00125.S. ALMA is a partnership of ESO (representing its member states), NSF (USA), and NINS (Japan), together with NRC (Canada), MOST and ASIAA (Taiwan), and KASI (Republic of Korea), in cooperation with the Republic of Chile. The Joint ALMA Observatory is operated by ESO, AUI/NRAO and NAOJ. P.G. acknowledges support from a Chalmers Initiative on Cosmic Origins (CICO) postdoctoral fellowship. J.C.T. acknowledges support from ERC Advanced Grant MSTAR, VR grant Fire from Ice, and NSF grant AST-2206450. We thank Jan Henrik Bredehøft for the helpful discussions. Y.Z. acknowledges the sponsorship from the Yangyang Development Fund. R.F. acknowledges support from the grants Juan de la Cierva FJC2021-046802-I, PID2020-114461GB-I00, and CEX2021-001131-S funded by MCIN/AEI/10.13039/501100011033, by “European Union NextGenerationEU/PRTR,” and by grant P20-00880 from the Consejería de Transformación Económica, Industria, Conocimiento y Universidades of the Junta de Andalucía. R.F. also acknowledges funding from the European Union’s Horizon 2020 research and innovation programme under the Marie Skłodowska-Curie grant agreement No. 101032092. D.M. and G.G. gratefully acknowledge the support of ANID through the BASAL project FB210003.

Appendix A

Moment 1 Maps of Different Species

Here, in Figure A1, we present first moment maps, i.e., showing the average velocity, of six of the species identified in G28.2.

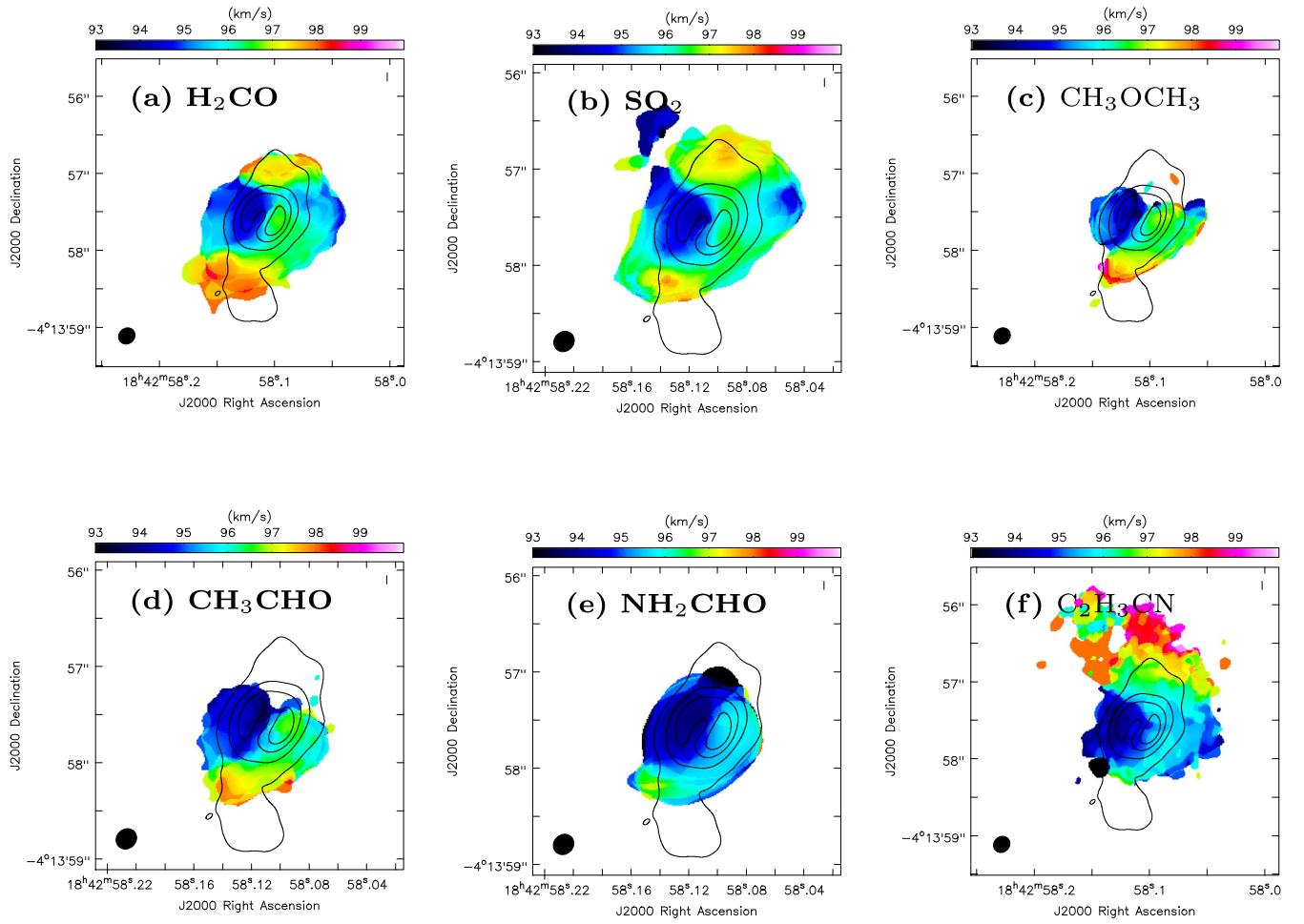


Figure A1. Moment 1 maps of (a) H_2CO ($E_{\text{up}} = 173$ K); (b) SO_2 ($E_{\text{up}} = 248$ K); (c) CH_3OCH_3 ($E_{\text{up}} = 253$ K); (d) CH_3CHO ($E_{\text{up}} = 93$ K); (e) NH_2CHO ($E_{\text{up}} = 60$ K); and (f) $\text{C}_2\text{H}_3\text{CN}$ ($E_{\text{up}} = 145$ K).

Appendix B LTE Model Spectra

In Figures B1–B3 we show observed spectra, together with synthetic model LTE spectra for HMC1, HMC2, and HMC3, respectively.

Observed (HMC1) + synthetic spectra

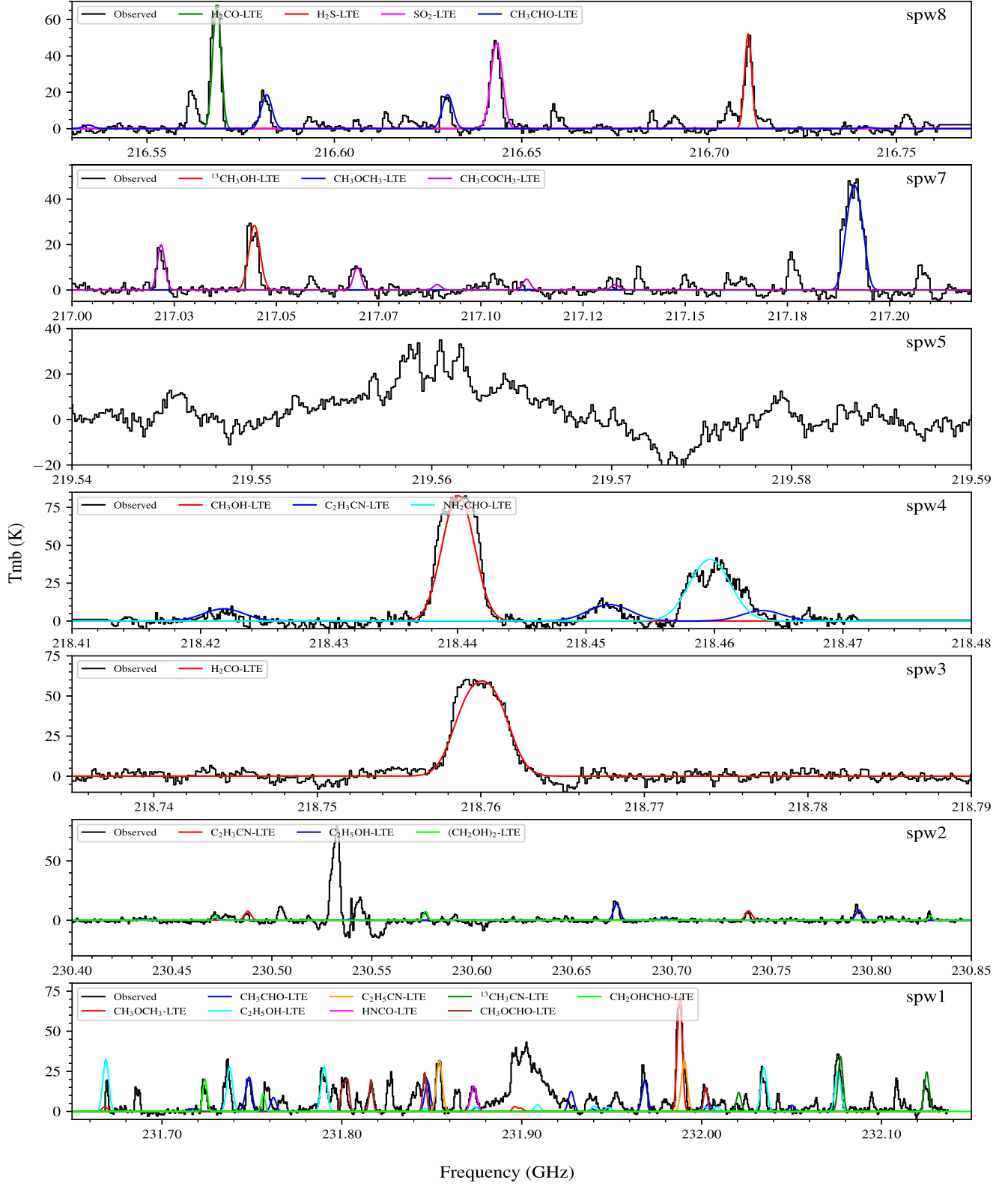


Figure B1. Continuum-subtracted spectra toward the G28.2 HMC1. Spectral windows 1, 2, 3, 4, 5, 7, and 8 are shown from bottom to top. The frequencies are in the source rest frame. Synthetic spectra of different species are overlaid on the top of observed spectra, as labeled.

Observed (HMC2) + synthetic spectra

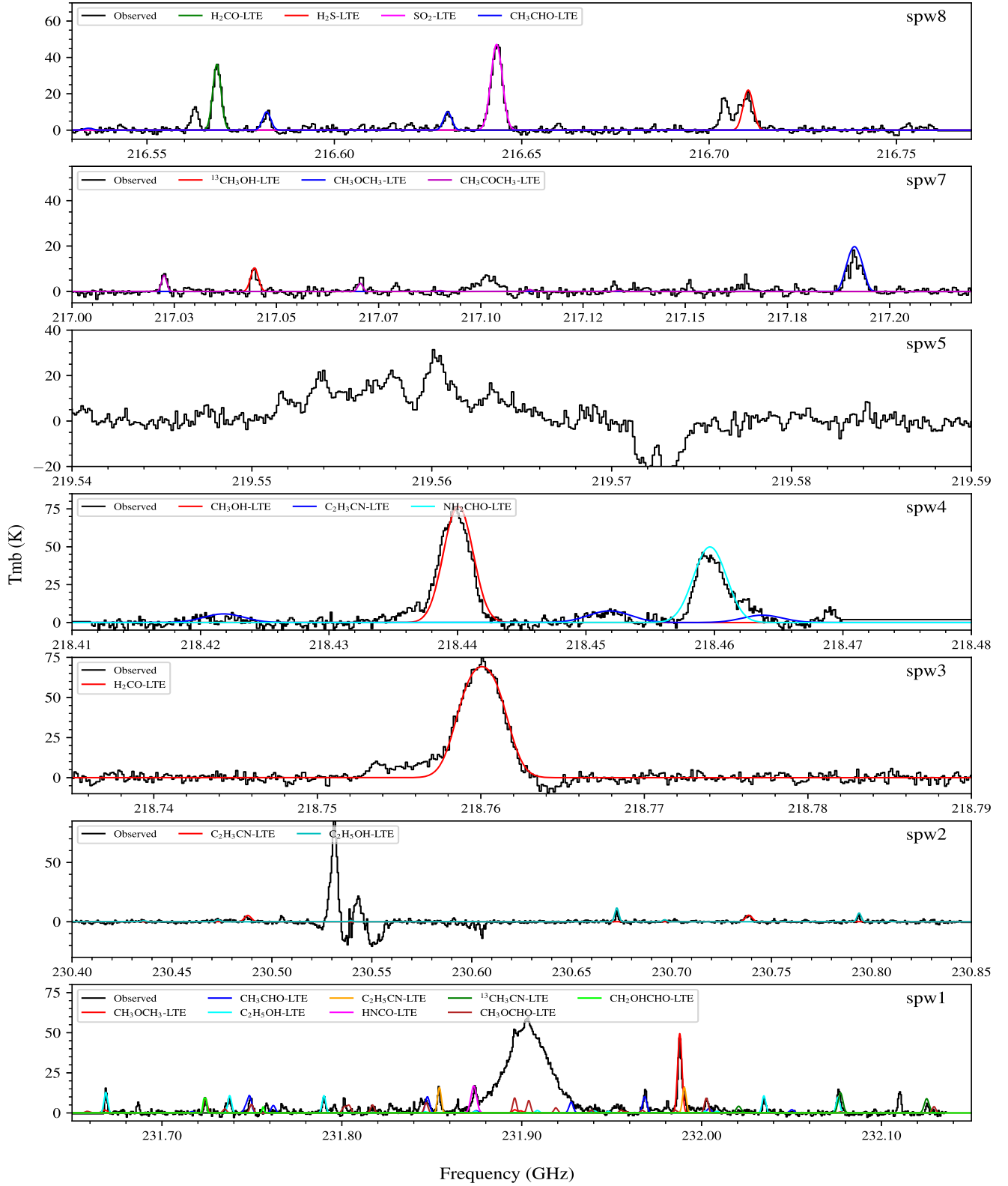


Figure B2. Continuum-subtracted spectra toward the G28.2 HMC2. Spectral windows 1, 2, 3, 4, 5, 7, and 8 are shown from bottom to top. The frequencies are in the source rest frame. Synthetic spectra of different species are overlaid on the top of observed spectra, as labeled.

Observed (HMC3) + synthetic spectra

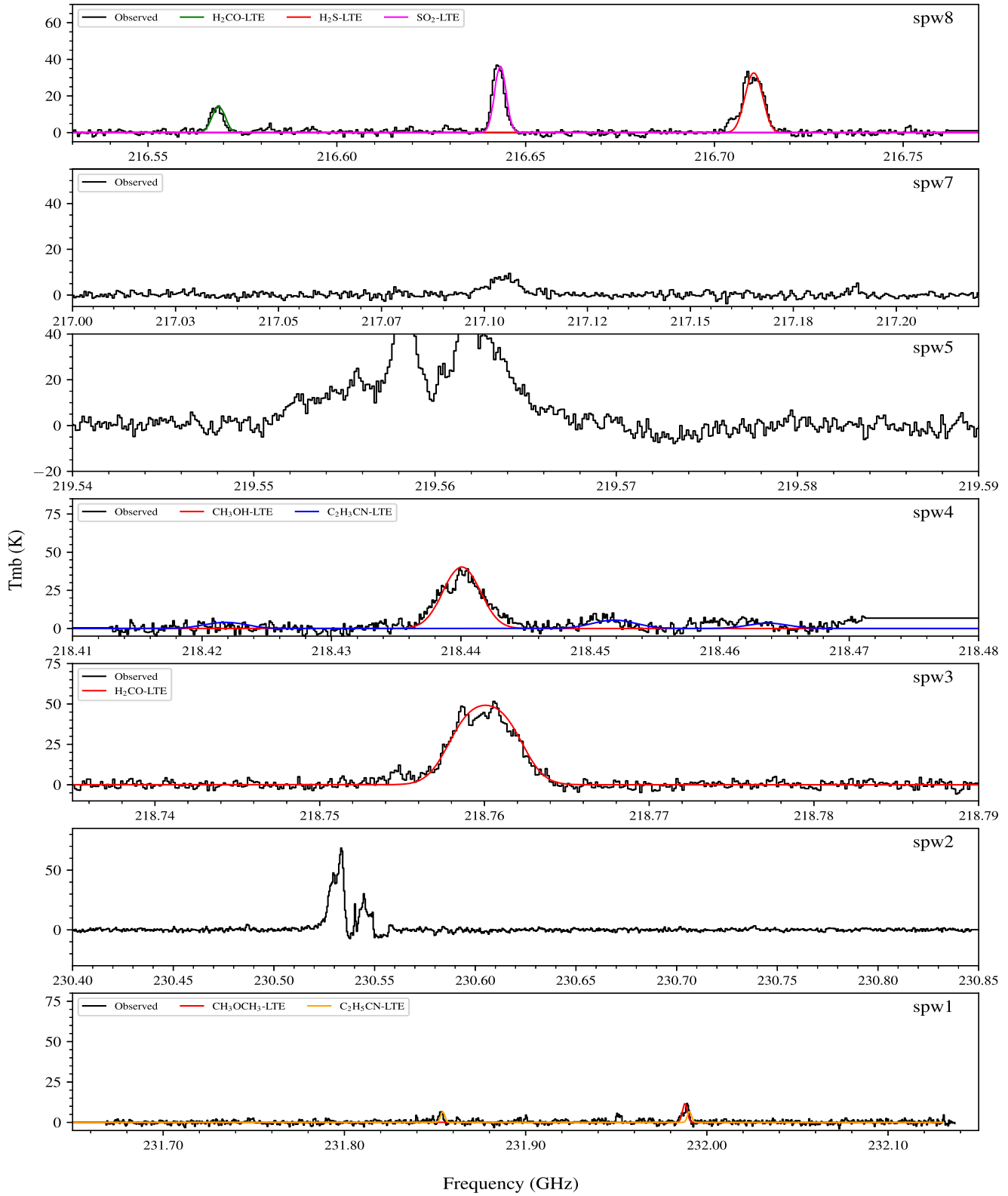


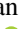


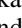
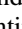






Figure B3. Continuum-subtracted spectra toward the G28.2 HMC3. Spectral windows 1, 2, 3, 4, 5, 7, and 8 are shown from bottom to top. The frequencies are in the source rest frame. Synthetic spectra of different species are overlaid on the top of observed spectra, as labeled.

ORCID iDs

Prasanta Gorai  <https://orcid.org/0000-0003-1602-6849>
 Chi-Yan Law  <https://orcid.org/0000-0003-1964-970X>
 Jonathan C. Tan  <https://orcid.org/0000-0002-3389-9142>
 Yichen Zhang  <https://orcid.org/0000-0001-7511-0034>
 Rubén Fedriani  <https://orcid.org/0000-0003-4040-4934>
 Kei E. I. Tanaka  <https://orcid.org/0000-0002-6907-0926>
 Mélisse Bonfand  <https://orcid.org/0000-0001-6551-6444>
 Giuliana Cosentino  <https://orcid.org/0000-0001-5551-9502>
 Diego Mardones  <https://orcid.org/0000-0002-5065-9175>
 Maria T. Beltrán  <https://orcid.org/0000-0003-3315-5626>
 Guido Garay  <https://orcid.org/0000-0003-1649-7958>

References

- Arce, H. G., Shepherd, D., Gueth, F., et al. 2007, in *Protostars and Planets V*, ed. B. Reipurth, D. Jewitt, & K. Keil (Tucson, AZ: Univ. Arizona Press), 245
- Bachiller, R., Pérez Gutiérrez, M., Kumar, M. S. N., & Tafalla, M. 2001, *A&A*, 372, 899
- Bally, J., Ginsburg, A., Forbrich, J., & Vargas-González, J. 2020, *ApJ*, 889, 178
- Balucani, N., Ceccarelli, C., & Taquet, V. 2015, *MNRAS*, 449, L16
- Belloche, A., Garrod, R. T., Müller, H. S. P., et al. 2009, *A&A*, 499, 215
- Belloche, A., Garrod, R. T., Müller, H. S. P., et al. 2019, *A&A*, 628, A10
- Belloche, A., Garrod, R. T., Müller, H. S. P., & Menten, K. M. 2014, *Sci*, 345, 1584
- Belloche, A., Meshcheryakov, A. A., Garrod, R. T., et al. 2017, *A&A*, 601, A49
- Blake, G. A., Sutton, E. C., Masson, C. R., & Phillips, T. G. 1987, *ApJ*, 315, 621
- Bonnell, I. A., Bate, M. R., & Zinnecker, H. 1998, *MNRAS*, 298, 93
- Bonnell, I. A., Clarke, C. J., Bate, M. R., & Pringle, J. E. 2001, *MNRAS*, 324, 573
- Boogert, A. C. A., Schutte, W. A., Helmich, F. P., Tielens, A. G. G. M., & Wooden, D. H. 1997, *A&A*, 317, 929
- Bouscasse, L., Csengeri, T., Belloche, A., et al. 2022, *A&A*, 662, A32
- Bredehöft, J. H., Böhrer, E., Schmidt, F., Borrmann, T., & Swiderek, P. 2017, *ESC*, 1, 50
- Brouillet, N., Despois, D., Lu, X. H., et al. 2015, *A&A*, 576, A129
- Caselli, P., Hasegawa, T. I., & Herbst, E. 1993, *ApJ*, 408, 548
- Cernicharo, J., Kisiel, Z., Tercero, B., et al. 2016, *A&A*, 587, L4
- Cesaroni, R., Hofner, P., Araya, E., & Kurtz, S. 2010, *A&A*, 509, A50
- Charnley, S. B. 1997, *ApJ*, 481, 396
- Charnley, S. B., Tielens, A. G. G. M., & Millar, T. J. 1992, *ApJL*, 399, L71
- Colzi, L., Rivilla, V. M., Beltrán, M. T., et al. 2021, *A&A*, 653, A129
- Combes, F., Gerin, M., Wootten, A., et al. 1987, *A&A*, 180, L13
- Csengeri, T., Belloche, A., Bontemps, S., et al. 2019, *A&A*, 632, A57
- de la Fuente, E., Porras, A., Trinidad, M. A., et al. 2020, *MNRAS*, 492, 895
- Enrique-Romero, J., Álvarez-Barcia, S., Kolb, F. J., et al. 2020, *MNRAS*, 493, 2523
- Feng, S., Beuther, H., Henning, T., et al. 2015, *A&A*, 581, A71
- Fontani, F., Pascucci, I., Caselli, P., et al. 2007, *A&A*, 470, 639
- Friedel, D. N., & Snyder, L. E. 2008, *ApJ*, 672, 962
- Garay, G., Mardones, D., Rodríguez, L. F., Caselli, P., & Bourke, T. L. 2002, *ApJ*, 567, 980
- Garrod, R. T. 2013, *ApJ*, 765, 60
- Garrod, R. T., Belloche, A., Müller, H. S. P., & Menten, K. M. 2017, *A&A*, 601, A48
- Garrod, R. T., & Herbst, E. 2006, *A&A*, 457, 927
- Garrod, R. T., Widicus Weaver, S. L., & Herbst, E. 2008, *ApJ*, 682, 283
- Gorai, P., Bhat, B., Sil, M., et al. 2020, *ApJ*, 895, 86
- Gorai, P., Das, A., Das, A., et al. 2017, *ApJ*, 836, 70
- Gorai, P., Das, A., Shimonishi, T., et al. 2021, *ApJ*, 907, 108
- Grudić, M. Y., Guszejnov, D., Offner, S. S. R., et al. 2022, *MNRAS*, 512, 216
- Haupt, K. A., Tarczay, G., & Lee, Y.-P. 2019, *JChS*, 141, 11614
- Herbst, E., & van Dishoeck, E. F. 2009, *ARA&A*, 47, 427
- Hernández-Hernández, V., Zapata, L., Kurtz, S., & Garay, G. 2014, *ApJ*, 786, 38
- Howk, J. C., Sembach, K. R., & Savage, B. D. 2006, *ApJ*, 637, 333
- Jørgensen, J. K., Belloche, A., & Garrod, R. T. 2020, *ARA&A*, 58, 727
- Jørgensen, J. K., Hogerheijde, M. R., Blake, G. A., et al. 2004, *A&A*, 415, 1021
- Klaassen, P. D., Wilson, C. D., Keto, E. R., et al. 2011, *A&A*, 530, A53
- Klaassen, P. D., Wilson, C. D., Keto, E. R., & Zhang, Q. 2009, *ApJ*, 703, 1308
- Kurtz, S., Cesaroni, R., Churchwell, E., Hofner, P., & Walmsley, C. M. 2000, in *Protostars and Planets IV*, ed. V. Mannings, A. P. Boss, & S. S. Russell (Tucson, AZ: Univ. Arizona Press), 299
- Law, C.-Y., Tan, J. C., Gorai, P., et al. 2022, *ApJ*, 939, 120
- Ligterink, N. F. W., Coutens, A., Kofman, V., et al. 2017, *MNRAS*, 469, 2219
- Luo, G., Feng, S., Li, D., et al. 2019, *ApJ*, 885, 82
- Mangum, J. G., Wootten, A., Loren, R. B., & Wadiak, E. J. 1988, *Molecular Clouds in the Milky Way and External Galaxies* (Berlin: Springer), 263
- Maret, S., Ceccarelli, C., Tielens, A. G. G. M., et al. 2005, *A&A*, 442, 527
- McKee, C. F., & Tan, J. C. 2003, *ApJ*, 585, 850
- McMullin, J. P., Waters, B., Schiebel, D., Young, W., & Golap, K. 2007, in *ASP Conf. Ser. 376, Astronomical Data Analysis Software and Systems XVI*, ed. R. A. Shaw, F. Hill, & D. J. Bell (San Francisco, CA: ASP), 127
- Milam, S. N., Savage, C., Brewster, M. A., Ziurys, L. M., & Wyckoff, S. 2005, *ApJ*, 634, 1126
- Minh, Y. C. 2016b, *JPhCS*, 728, 052007
- Mondal, S. K., Gorai, P., Sil, M., et al. 2021, *ApJ*, 922, 194
- Mues, M. 2021, *Masters thesis*, Bremen Univ.
- Müller, H. S. P., Schlöder, F., Stutzki, J., & Winnewisser, G. 2005, *JMoSt*, 742, 215
- Müller, H. S. P., Thorwirth, S., Roth, D. A., & Winnewisser, G. 2001, *A&A*, 370, L49
- Myers, A. T., McKee, C. F., Cunningham, A. J., Klein, R. I., & Krumholz, M. R. 2013, *ApJ*, 766, 97
- Ossenkopf, V., & Henning, T. 1994, *A&A*, 291, 943
- Pagani, L., Bergin, E., Goldsmith, P. F., et al. 2019, *A&A*, 624, L5
- Palumbo, M. E., Geballe, T. R., & Tielens, A. G. G. M. 1997, *ApJ*, 479, 839
- Palumbo, M. E., Tielens, A. G. G. M., & Tokunaga, A. T. 1995, *ApJ*, 449, 674
- Peng, T. C., Despois, D., Brouillet, N., et al. 2013, *A&A*, 554, A78
- Pickett, H. M., Poynter, R. L., Cohen, E. A., et al. 1998, *JQST*, 60, 883
- Podio, L., Lefloch, B., Ceccarelli, C., Codella, C., & Bachiller, R. 2014, *A&A*, 565, A64
- Qin, S.-L., Huang, M., Wu, Y., Xue, R., & Chen, S. 2008, *ApJL*, 686, L21
- Rivilla, V. M., Beltrán, M. T., Cesaroni, R., et al. 2017, *A&A*, 598, A59
- Rolfes, R., Schilke, P., Zhang, Q., & Zapata, L. 2011, *A&A*, 536, A33
- Ruad, M., Loison, J. C., Hickson, K. M., et al. 2015, *MNRAS*, 447, 4004
- Savage, B. D., & Sembach, K. R. 1996, *ARA&A*, 34, 279
- Sewilo, M., Churchwell, E., Kurtz, S., Goss, W. M., & Hofner, P. 2004, *ApJ*, 605, 285
- Sewilo, M., Churchwell, E., Kurtz, S., Goss, W. M., & Hofner, P. 2008, *ApJ*, 681, 350
- Singh, S. K., Fabian Kleimeier, N., Eckhardt, A. K., & Kaiser, R. I. 2022, *ApJ*, 941, 103
- Skouteris, D., Balucani, N., Ceccarelli, C., et al. 2019, *MNRAS*, 482, 3567
- Sollins, P. K., Zhang, Q., Keto, E., & Ho, P. T. P. 2005, *ApJ*, 631, 399
- Suzuki, T., Ohishi, M., Saito, M., et al. 2018, *ApJS*, 237, 3
- Tan, J. C., Beltrán, M. T., Caselli, P., et al. 2014, in *Protostars and Planets VI*, ed. H. Beuther et al. (Tucson, AZ: Univ. Arizona Press), 149
- Taniguchi, K., Plunkett, A., Herbst, E., et al. 2020, *MNRAS*, 493, 2395
- Taquet, V., Wiström, E. S., & Charnley, S. B. 2016, *ApJ*, 821, 46
- Tiefrunk, A., Pineau des Forets, G., Schilke, P., & Walmsley, C. M. 1994, *A&A*, 289, 579
- van der Tak, F. F. S. 2004, in *IAU Symp. 221, Star Formation at High Angular Resolution*, ed. M. G. Burton, R. Jayawardhana, & T. L. Bourke (San Francisco, CA: ASP), 59
- Vastel, C., Bottinelli, S., Caux, E., Glorian, J. M., & Boiziot, M. 2015, *SF2A-2015: Proc. of the Annual Meeting of the French Society of Astronomy and Astrophysics*, ed. F. Martins et al. (Paris: Société Française d'Astronomie et d'Astrophysique), 313
- Vazart, F., Ceccarelli, C., Balucani, N., Bianchi, E., & Skouteris, D. 2020, *MNRAS*, 499, 5547
- Wakelam, V., Caselli, P., Ceccarelli, C., Herbst, E., & Castets, A. 2004, *A&A*, 422, 159
- Walsh, A. J., Macdonald, G. H., Alvey, N. D. S., Burton, M. G., & Lee, J. K. 2003, *A&A*, 410, 597
- Woods, P. M., Occhiogrosso, A., Viti, S., et al. 2015, *MNRAS*, 450, 1256
- Zhang, S., Zavagno, A., López-Sepulcre, A., et al. 2021, *A&A*, 646, A25
- Zhang, Y., Tan, J. C., Tanaka, K. E. I., et al. 2019, *NatAs*, 3, 517